

## Cauliflower mosaic virus P6 inclusion body formation: A dynamic and intricate process

Roberto Alers-Velazquez<sup>a</sup>, Sarah Jacques<sup>a</sup>, Clare Muller<sup>a</sup>, Jennifer Boldt<sup>b</sup>, James Schoelz<sup>c</sup>, Scott Leisner<sup>a,\*</sup>

<sup>a</sup> Department of Biological Sciences, University of Toledo, 2801 West Bancroft Street, Mail Stop 601, Toledo, OH, 43606, USA

<sup>b</sup> USDA-Agricultural Research Service, Application Technology Research Unit, 2801 West Bancroft Street, Mail Stop 604, Toledo, OH, 43606, USA

<sup>c</sup> Division of Plant Sciences, University of Missouri, Columbia, MO, 65211, USA

### ARTICLE INFO

#### Keywords:

LifeAct  
Latrunculin B  
GFP-250  
Liquid-liquid phase separation  
Nonmembranous organelles  
Pararetrovirus  
Particle tracking

### ABSTRACT

During an infection, *Cauliflower mosaic virus* (CaMV) forms inclusion bodies (IBs) mainly composed of viral protein P6, where viral activities occur. Because viral processes occur in IBs, understanding the mechanisms by which they are formed is crucial. FL-P6 expressed in *N. benthamiana* leaves formed IBs of a variety of shapes and sizes. Small IBs were dynamic, undergoing fusion/dissociation events. Co-expression of actin-binding polypeptides with FL-P6 altered IB size distribution and inhibited movement. This suggests that IB movement is required for fusion and growth. A P6 deletion mutant was discovered that formed a single large IB per cell, which suggests it exhibited altered fusion/dissociation dynamics. Myosin-inhibiting drugs did not affect small IB movement, while those inhibiting actin polymerization did. Large IBs colocalized with components of the aggresome pathway, while small ones generally did not. This suggests a possible involvement of the aggresome pathway in large IB formation.

### 1. Introduction

During the course of an infection, viruses often induce the formation of structures within cells that promote propagation of the pathogen (Martelli and Russo, 1977; Moshe and Gorovits, 2012; Novoa et al., 2005). These structures go by a variety of names [e.g., replication factories, viroplasm, inclusion bodies (IBs)]. Viral IBs may form in the nucleus, within the cytoplasm, or in association with cellular membranous organelles.

Intriguingly, some viruses may induce formation of more than one type of IB, each needed to perform different functions. For example, *Cauliflower mosaic virus* (CaMV) can form two different types of IBs: those comprised of mainly viral protein P2 and those composed of primarily viral protein P6 (Bak et al., 2013; Espinoza et al., 1991; Fujisawa et al., 1967; Martelli and Castellano, 1971). The P2 IBs are cytoplasmic, appear electron-lucent in electron micrographs and play a role in aphid transmission of CaMV (Espinoza et al., 1991; Khelifa et al., 2007; Martinieri et al., 2009). P6 IBs are cytoplasmic, electron-dense structures equivalent to virion factories reported for other viruses that are required for infection (Daubert et al., 1983; Hull and Covey, 1985; Kobayashi

et al., 1998; Lutz et al., 2015; Melcher et al., 1986; Schoelz and Leisner, 2017; Shockey et al., 1980).

CaMV is a plant pararetrovirus (Haas et al., 2002; Hohn and Rothnie, 2013; Hull and Covey, 1985; Khelifa et al., 2010; Lutz et al., 2015; Schoelz and Leisner, 2017). The 50 nm in diameter icosahedral virions composed of the capsid protein (P4), either with or without the linker protein (P3), can be introduced into plant cells by mechanical damage, or naturally by insect vectors (aphids). Once inside a cell, virions are targeted to the nucleus through the nuclear localization signal (NLS) located on P4. Viral DNA then enters the nucleus where it is transcribed to produce two RNAs, the 19S and 35S, which then exit the nucleus. The 19S transcript serves as an mRNA for the synthesis of P6. The 35S transcript serves in a dual role as an mRNA to synthesize all CaMV proteins and as a template for reverse transcription to generate viral DNA genomes. The P6 produced from the CaMV RNAs is then assembled into a variety of IBs of different shapes and sizes. P6 IBs, where viral protein synthesis, genome replication and virion assembly are thought to occur, are the focus of this paper. From here on, IBs will refer only to those structures mainly composed of P6. As the infection progresses, chronically-infected cells usually contain a single large perinuclear IB

\* Corresponding author.

E-mail address: [Scott.Leisner@utoledo.edu](mailto:Scott.Leisner@utoledo.edu) (S. Leisner).

<https://doi.org/10.1016/j.virol.2020.10.003>

Received 20 August 2020; Received in revised form 13 October 2020; Accepted 18 October 2020

Available online 30 October 2020

0042-6822/© 2020 The Authors.

Published by Elsevier Inc.

This is an open access article under the CC BY-NC-ND license

(<http://creativecommons.org/licenses/by-nc-nd/4.0/>).

(Shepherd, 1976).

Since P6 is the major IB component, it was important to examine which portions of the protein are involved in self-association. P6 contains four regions capable of binding to the full-length protein, previously termed D1–D4 (Fig. 2A) (Haas et al., 2005; Li and Leisner, 2002). Data in the literature suggest that viruses encoding P6s lacking any one of these regions would be non-infectious (Kobayashi and Hohn, 2004; Lutz et al., 2015). D1 consists of P6 amino acids 1–110. This region contains nuclear export signals and regions important for the formation of larger IBs, because when certain amino acid substitutions are made, only small IBs form (Geldreich et al., 2017; Haas et al., 2015). D2 consists of P6 amino acids 156–253 (Li and Leisner, 2002) and overlaps with an important P6 function: translational transactivation (TAV). P6, via its TAV function (localized to amino acids 111–242), is able to facilitate translation of the multiple open reading frames on the polycistronic viral genomic 35S RNA (Bonneville et al., 1989; De Tapia et al., 1993; Gowda et al., 1989). This same region also binds to large ribosomal subunit proteins (Bureau et al., 2004; Leh et al., 2000), possibly facilitating TAV function and promoting the recruitment of ribosomes surrounding the IB (Martelli and Castellano, 1971; Shepherd, 1976). D3 (amino acids 249–379) (Li and Leisner, 2002) contains two non-sequence-specific RNA-binding domains (De Tapia et al., 1993), the first of which also binds to a ribosomal subunit protein, and translation initiation factor eIF-3g (Park et al., 2001). D4 (amino acids 414–520) (Li and Leisner, 2002) contains a putative zinc-finger required for infectivity (De Tapia et al., 1993; Turner et al., 1996). While regions playing a role in P6 self-association have been identified (Haas et al., 2005; Li and Leisner, 2002), their role in IB formation was unclear.

The molecular mechanisms by which P6 forms cytoplasmic aggregates are currently poorly understood. One possibility by which this might happen is through liquid-liquid phase separation (Alberti and Dormann, 2019; Cuevas-Velazquez and Dinneny, 2018; Hyman et al., 2014) to form a membraneless compartment (MC). Cells can form a variety of MCs where they mediate a variety of specific functions ranging from ribosomal subunit biosynthesis to regulating mRNA stability and response to stress. Many MCs are formed by mixtures of proteins and RNA, and they possess the properties of a liquid droplet. Hence, MCs appear to form a liquid phase separate from that of the bulk cytoplasm (or nucleoplasm). This process has been termed liquid-liquid phase separation and these liquid droplets possess a number of interesting properties (Hyman et al., 2014). The liquid droplets are generally spherical. When two or more droplets contact each other, they can fuse and eventually revert to a rounded shape. Droplet shape is affected when exposed to shear flows around it. Liquid droplets are able to exchange materials with their environment. Because droplets behave as though they are a liquid, their components are free to move within the droplet. The interior of the liquid droplets can convert to a more solid or gel-like structure through a process termed “Molecular Aging” (Alberti and Dormann, 2019). Several types of MCs can be dissociated when treated with 1,6-hexanediol (Chong et al., 2018) indicating that the droplets are held together via hydrophobic interactions. The proteins that make up these liquid-liquid phase-separated droplets often contain multiple sites for interaction with other proteins and RNA (Alberti and Dormann, 2019; Cuevas-Velazquez and Dinneny, 2018; Hyman et al., 2014) and as a result they can be predicted in silico (PSPredictor; Sun et al. (2019)).

P6 IBs are mobile within plant cells (Harries et al., 2009). The small, highly-mobile IBs co-localize with Talin-DsRed-decorated actin filaments. Actin-based movements can occur via two separate routes: myosins and actin monomer polymerization (Cramer et al., 1994; Svitkina, 2018). Plant myosins are involved in a variety of processes including the movement of mitochondria (Van Gestel et al., 2002). Plants contain two myosin gene families: VIII and XI, both of which are most closely related to animal cell myosin V (Tominaga and Nakano, 2012). In animal and plant cells, myosin-based movements can be inhibited by 2,3-butanedione monoxime (BDM) (Samaj et al., 2000). BDM inhibits the ATPase activity of myosins, interfering with cytoplasmic streaming and

mitochondrial movement in plant cells (Tominaga et al., 2000; Van Gestel et al., 2002). Another myosin-inhibitor, Blebbistatin (BL), interferes with phosphate release from the motor domain of myosin II and is a more specific drug than BDM (Kovacs et al., 2004).

It is possible that the highly-mobile small IBs could also move via actin filament polymerization. Poxvirus virions move intracellularly via this mechanism, as do certain bacteria (Haglund and Welch, 2011). Among its many binding partners, P6 interacts with the Chloroplast Unusual Positioning-1 (CHUP1) protein (Angel et al., 2013). CHUP1 permits movement of chloroplasts in plant cells in response to light (Wada and Kong, 2018). A model has been proposed in which CHUP1 attaches to the outer membrane of chloroplasts and moves these organelles by actin filament polymerization. Because P6 binds CHUP1 (Angel et al., 2013) it is possible that IBs also move via a similar mechanism.

Various actin-perturbing drugs also offer interesting information regarding how plant cells move various components (Holzinger and Blaas, 2016) and have shed light on some aspects of IB formation (Harries et al., 2009). Latrunculin B (LatB) rapidly binds to actin monomers, thereby inhibiting polymerization, and also damages actin filaments (Chen et al., 2007). LatB dramatically reduced CaMV propagation and inhibited movement of small IBs (Harries et al., 2009).

While small IBs appear to actively move along actin filaments, large IBs are significantly less mobile and are associated with microtubules (Harries et al., 2009). Large IBs are likely formed through aggregation of small IBs (Schoelz and Leisner, 2017; Shepherd, 1976). The association of large IBs with microtubules is reminiscent of structures called aggresomes (Johnston et al., 1998; Kopito, 2000). When cells over-express a misfolded protein it is often concentrated, bundled together, and moved along microtubules to accumulate in a perinuclear location, thereby forming an aggresome. The cell may try to refold aggresomal proteins via molecular chaperones such as HSC70, either on their voyage to, or in their final destination near the nucleus. To fuel HSC70-mediated refolding, the protein packets and aggresomes are usually surrounded by mitochondria, which presumably supply ATP. Eventually, the aggresome may be surrounded by intermediate filaments to keep the misfolded protein localized, or it may interact with autophagy pathway components for degradation. Thus, it is possible that large IBs may interact with the aggresome pathway.

In summary, IBs are structures important for CaMV infection and how they form is still poorly understood. To gain further insight into IB formation, we took a four-pronged approach: 1) examined the possible involvement of liquid-liquid phase separation; 2) determined the role of each P6 self-association domain; 3) examined the role of the actin cytoskeleton in more detail; and 4) tested whether large IBs are associated with the aggresome pathway.

## 2. Materials and methods

### 2.1. Expression constructs

The vector expressing the nuclear Cajal body marker, coilin-fused mCherry (Kim et al., 2007), was obtained from TAIR (The Arabidopsis Information Resource; Columbus, OH; Berardini et al. (2015)). Vectors expressing proteins labeling the nucleus (NLS-mCherry-GUS), the plasma membrane (AtPIP2a-mCherry; *Arabidopsis thaliana* plasma membrane intrinsic protein 2a), actin (LifeAct-mCherry), and mitochondria (mCherry-COX4) are described in Ivanov and Harrison (2014). The first three clones were obtained from Addgene (Watertown, MA), while the last one was obtained from TAIR. The marker for microtubules, MAP4-mCherry, was a kind gift from Dr. Björn Krenz from the Leibniz Institute DSMZ, Department of Virology, and described in (Krapp et al., 2017). The Talin-DsRed and eIF3g-RFP constructs have been previously described (Angel et al., 2013; Harries et al., 2009).

The full-length cDNA for *A. thaliana* HSC70 (accession number AT5G02500) was obtained from TAIR. The cDNA clone was used as a

template to generate PCR products encoding HSC70 using primers indicated in Table S1. The PCR products were subsequently inserted into the entry vector pENTR/D-TOPO (ThermoFisher Scientific, St. Louis, MO) according to the manufacturer's specifications. This and all other constructs generated in this paper were confirmed by sequencing performed by Genewiz (South Plainfield, NJ).

A vector containing the aggresomal marker GFP-250 was a kind gift from Dr. Elizabeth Sztul from the Department of Cell Biology at the University of Alabama at Birmingham. GFP-250 consists of GFP fused to the N-terminal 252 amino acids of General Vesicular Transport Factor p115 (Garcia-Mata et al., 1999). The DNA segment encoding GFP-250 was amplified using the primers indicated in Table S1 employing pEGFP-C2 as a template. The PCR product was then inserted into pENTR/D-TOPO according to the manufacturer's specifications.

A clone of full-length CM1841 gene VI (encoding P6) inserted into pENTR/D-TOPO was generated previously (Lutz et al., 2015). Gene VI deletions lacking the portions encoding D1 or D4 were generated by PCR using the primers in Table S1 using pCaMV10 (Gardner et al., 1981) as a template. These PCR products were then individually inserted into pENTR/D-TOPO according to the manufacturer's specifications. Gene VI lacking the portion encoding the D3 region was generated by PCR using the primers indicated in Table S1 and the pCaMV10-NcoI-DE clone (Li and Leisner, 2002) as a template, respectively. These PCR products were then individually inserted into pENTR/D-TOPO using the manufacturer's specifications.

The DNA segments encoding P6 and lacking the D2 region were made by Gibson Assembly using the primers in Table S1. The 5' fragment for P6 $\Delta$ D2 was PCR amplified using pCaMV10 (Gardner et al., 1981) as the template and the primers P6GA-Start-1F and P6D2GA-1R (501 bp), while the 3' fragment used pCaMV10 as the template and the primers P6D2GA-2F and P6GA-END-2R (837 bp). The vector pUC19 was digested with *Sma*I (ThermoFisher Scientific) according to the manufacturer's specifications. The appropriate 5' and 3' fragments were mixed with digested pUC19 and incubated with the Gibson Assembly Reaction Master Mix according to the manufacturer's (New England Biolabs, Ipswich, MA) specifications. The assembled plasmids were then confirmed by sequencing. All sequencing was performed by Genewiz (South Plainfield, NJ). The confirmed constructions were used as templates for PCR amplification using the 6SL-1F and 6D4NoStop-R primers and the amplicons were inserted into pENTR/D-TOPO according to the manufacturer's specifications.

Once inserted into pENTR/D-TOPO, the protein coding sequences for all genes used in this study were then mobilized into plant binary expression vectors encoding the appropriate fluorescent protein tags. Mobilization was accomplished using the L/R Clonase II enzyme mix (ThermoFisher Scientific), employing Gateway® technology according to the manufacturer's specifications. Genes encoding proteins to be tagged with GFP were inserted into pSITE-2NB (Chakrabarty et al., 2007) while those to be tagged with RFP were inserted into pSITE-4NB. The vector expressing CM1841 P6 without a stop codon fused at its C-terminus to the N-terminus of GFP was previously reported (Lutz et al., 2015). For the remainder of the paper we refer P6-GFP as FL-P6. The GFP-250 coding sequences were inserted into pSITE-0A (Chakrabarty et al., 2007). All clones were confirmed by sequencing.

## 2.2. Plant growth conditions and agroinfiltration assay

*Nicotiana benthamiana* seeds were sown on soilless growth media supplemented with nutrient solution (Li et al., 2008). Plants were then maintained in a growth chamber (25 °C, 45% humidity) under a 16 h light (130  $\mu\text{mol m}^{-2} \text{s}^{-1}$ ) and 8 h dark cycle.

Constructs were introduced into *Agrobacterium tumefaciens* strain AGL1 by electroporation (Mattanovich et al., 1989). *A. tumefaciens* harboring the constructs were infiltrated with a 1 ml needleless syringe into the leaves of 4–6-week old *N. benthamiana*. For expression of a single fluorescent protein, the *A. tumefaciens* harboring plasmid

encoding that polypeptide was mixed in equal quantities with *A. tumefaciens* containing a vector expressing P19 of *Tomato bushy stunt virus* (Angel et al., 2011). For expression of two fluorescent proteins, *A. tumefaciens* harboring vectors expressing each of those proteins along with the plasmid expressing P19 were mixed in an equal ratio as described by Lutz et al. (2015). Each experiment was conducted a minimum of three times, each time infiltrating three leaves per plant. For each co-expression, the constructs and their appropriate controls were infiltrated on the same leaf on opposite sides of the midrib.

## 2.3. Confocal microscopy

Three days following inoculation, infiltrated leaf sections were excised using a 3/16" Cork Borer and mounted on a 35 mm glass bottom dish with a 14 mm microwell and #1.5 (.16–.19 mm thickness) cover-glass (Fisher Scientific). A 12 mm #1.5 coverslip (Thomas Scientific) was placed on top of the tissue inside the plate to flatten the sample for microscopy. Leaf sections were then examined using an Olympus IX71 unit equipped with a CSU-X1 spinning disk unit (Yokogawa, Japan). Piezo Z Top plate (ASI, USA) was used for acquiring Z-series. Images were captured utilizing an EMCCD camera (IXON-897, Andor) controlled by iQ3.0 (Andor). Fluorescent proteins were excited with lasers 488 nm and 561 nm. A 40x oil immersion objective lens or a 20X air objective lens if indicated (Olympus, Japan), was utilized to acquire images. Images and movies taken were Z-stacks (32 planes, with a 1  $\mu\text{m}$  distance between planes) or as single planes if indicated.

## 2.4. Image processing

Images, movies and size distribution measurements were processed using the Fiji software (Schindelin et al., 2012). Background noise removal and size distribution of P6 IBs images and movies were quantified and processed as described by Labno (2020). Co-localizations were measured by line scan analysis as described by Aulas et al. (2017).

## 2.5. Statistical analysis

Size distribution analysis was performed using Multiple *t*-test followed by Holm-Šidák correction for multiple comparisons (GraphPad Prism version 8.0.0 for Windows, GraphPad Software, San Diego, CA, USA, [www.graphpad.com](http://www.graphpad.com)).

## 2.6. Measurement of P6 inclusion body movement

IB velocity measurements were determined from microscopy Z-stack exposure videos using a neural network single particle tracking program, Neural Net Tracker (Newby et al., 2018). IB coordinates were individually tracked for 60 s in 2 s intervals. Two-dimensional coordinate data and the pixel signal radius of each particle were recorded by Neural Net Tracker for each time interval. To determine the visible particle area, particle radius according to Neural Net Tracker metadata was converted to  $\mu\text{m}^2$  using  $A = \pi r^2$  and averaged for each particle. Radius means were used to calculate the visible area in micrometers for each particle tracked in the compressed two-dimensional images. Particle velocity was determined using coordinate data from Neural Net Tracker. Euclidian distance was calculated for each second of travel, and mean velocity was determined as the average distance traveled in micrometers per second for each particle. Plots comparing particle velocity and particle size were created in R version 4.0.2 (R-Core, 2020) using the graphics package ggplot2 (Hadley, 2016). A threshold of "lower mobility" was set to 2.5  $\mu\text{m s}^{-1}$  based on the average velocity of the largest particles observed ( $>20 \mu\text{m}^2$ ) which are known to be the least mobile (Harries et al., 2009). The percentage of particles traveling faster than 2.5  $\mu\text{m s}^{-1}$  on average (particles with "higher mobility") and particles slower than 2.5  $\mu\text{m s}^{-1}$  on average (particles with "lower mobility") are reported for each treatment.

## 2.7. Protein expression analysis of P6 mutants

To examine mutant P6 protein levels, *N. benthamiana* leaves were agroinfiltrated and harvested as described in (Angel et al., 2013) with minor modifications to the extraction buffer and centrifugation step. Briefly, leaves harvested were ground at a 1:2 ratio (wt./vol.) with an extraction buffer (25 mM Tris pH 7.5, 150 mM NaCl, 1 mM DTT, 1 mM PMSF, 1X Pierce Protease Inhibitor EDTA-free tablet (according to the manufacturer's specifications), 1X Pierce Phosphatase Inhibitor tablet (Thermo Fisher Scientific, Waltham, MA; according to the manufacturer's specifications), 1 mM CaCl<sub>2</sub>, 0.1% Triton X-100, 5% Glycerol and .5% NP40). The extract was centrifuged at 2000×g for 10 min at 4 °C. The supernatant was then mixed with an equal volume of 2X SDS-PAGE loading buffer and boiled for 10 min. SDS-PAGE was performed as described in Lutz et al. (2015). FL-P6 and Actin were detected by incubating the membranes overnight with a Polyclonal anti-GFP (1:500) or a monoclonal anti-Actin (1:2000) antibody. These antibodies were

purchased from Thermo Fisher Scientific, Catalog number PA1-980A and Abmart (Berkley Heights, NJ) Catalog number M20009 respectively. After incubation with primary antibodies, blots were washed with 1X TBST for 10 min and repeated 3 times. For detection of FL-P6 and Actin, membranes were incubated for 4 h with anti-rabbit (1:5000) and anti-mouse (1:5000) antibodies, respectively. Both anti-rabbit and anti-mouse secondary antibodies were purchased from Thermo Fisher Scientific (Catalog number A27036 and Catalog number A28177, respectively).

## 2.8. Drug treatments

To address whether movement is myosin-dependent, two different drugs were tested: Blebbistatin (BL) Sigma Aldrich, St. Louis, MO) and 2,3-butanedione monoxime (BDM) (Abcam, Cambridge, UK). BL was infiltrated into leaves at a concentration of 50 μM in DMSO from a stock of 2 mM. BDM was infiltrated at a concentration of 100 μM as described

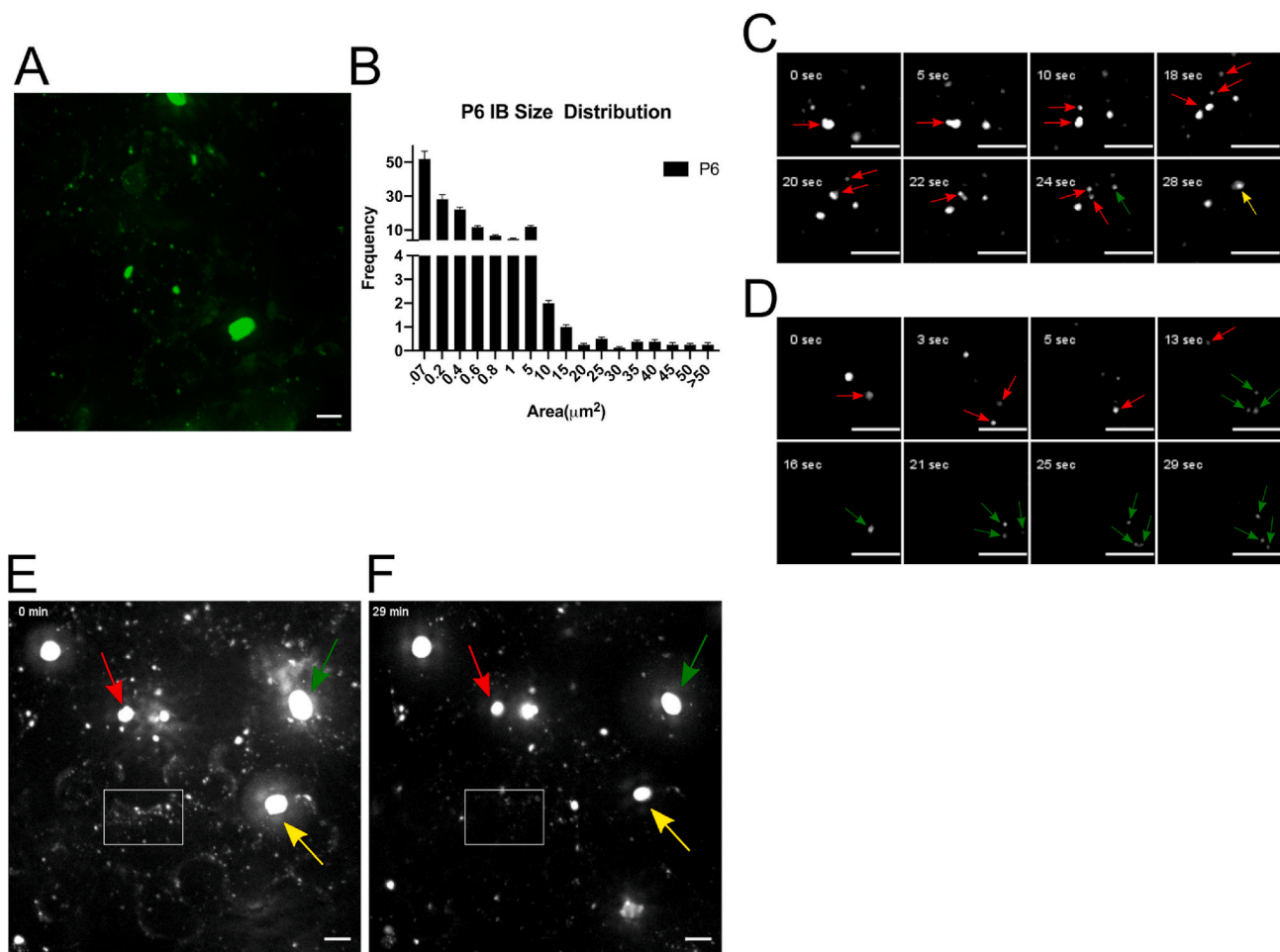


**Fig. 1. Cauliflower mosaic virus (CaMV) gene VI product (P6) forms inclusion bodies (IBs) of different sizes and shapes that are dynamic and affected by a phase separation reagent.**

*Nicotiana benthamiana* leaves agroinfiltrated with a construct expressing CaMV CM1841 P6 fused to the N-terminus of GFP, for three days. A. FL-P6 IB Z-Stack image obtained by spinning disc confocal fluorescence microscopy. B. Size distribution of IBs produced by FL-P6 (number of IBs versus IB area in square micrometers) based on six independent images. C. Time series of dissociation and fusion of IBs. The IBs marked by red arrows show variation in shape and dissociation from the same IB, the larger IB (20 s, lower red arrow) splits into two smaller IBs (22 s, red arrows) that then fuse together with another IB (24 s, green arrow) to produce a single larger IB (28 s, yellow arrow). This time series is derived from Movie S1A from area marked with a yellow box. D. Time series (shown as a single plane image) of IBs separating yet remaining correlated. The IB marked by a red arrow splits into two IBs. Three IBs marked by green arrows fuse together to produce a single IB that then splits into three IBs that remain near each other, but do not immediately fuse. This time series is derived from Movie S1B from area marked with a white box. FL-P6 IBs before E. and after 30 min of treatment with 1,6 hexanediol F. The area in the white boxes illustrates the dissolution of small IBs before and after the 30 min treatment. The colored arrows in E. and F. indicate three larger IBs that decreased in size after treatment as described in the narrative. C.-D. images were despeckled using Fiji. Scale bars in all images represent 10 μm. (For interpretation of the references to color in this figure legend, the reader is referred to the Web version of this article.)

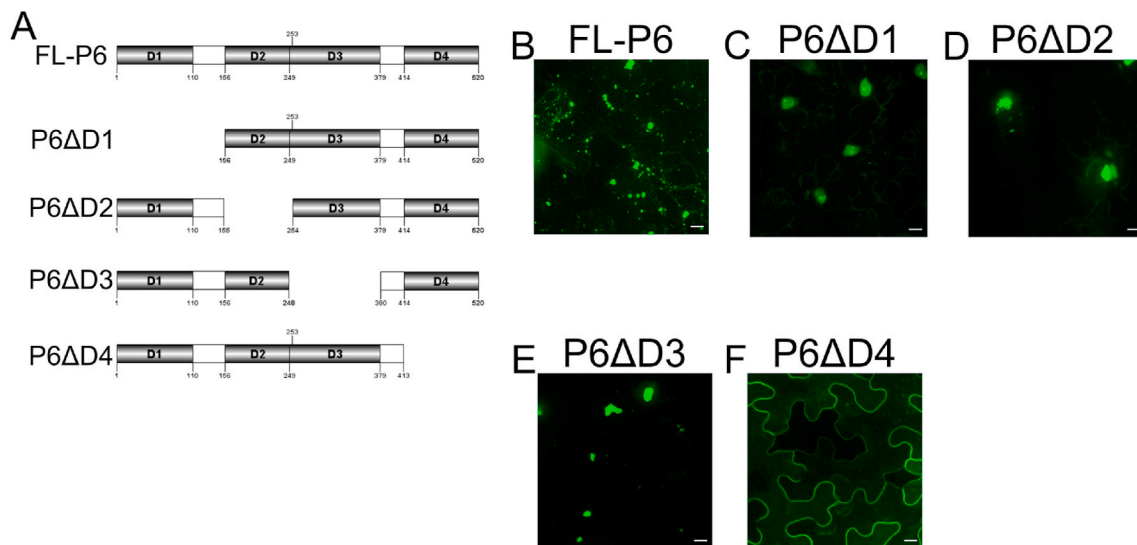


**Fig. 2. Effects of P6 interaction domain deletions on IB formation.**

A. Schematic diagram of the four self-association domains of P6 (FL-P6) (Li and Leisner, 2002) along with the deletion of each domain in the P6 derivatives. Gray boxes represent each domain (labeled D1-D4); white boxes, intervening regions; numbers above and below are amino acid positions in P6. B-F. Z-Stack images of fluorescent green foci formed by wild-type FL-P6 B, and each of the deletion mutants as indicated. Scale bar in images represent 10  $\mu\text{m}$ . (For interpretation of the references to color in this figure legend, the reader is referred to the Web version of this article.)

in (Feng et al., 2016). Mitochondria move along actin filaments via myosins (Van Gestel et al., 2002). Therefore, mitochondrial movement was used as a control for ensuring that BL and BDM were entering cells and inhibiting myosin activity.

To address the role of actin on IB formation we used Latrunculin B (LatB) (VWR International, Radnor, PA). Treatments with the actin destabilizing drug LatB were performed as described by Harries et al. (2009) with one modification; leaves were infiltrated with 5  $\mu\text{M}$  LatB and incubated 5 h. As a control the other half of the leaf was infiltrated with an equal dilution of DMSO as the LatB treatment.

For assaying phase separation, leaves were infiltrated with 10% 1,6 Hexanediol/10  $\mu\text{g}$  Digitonin (Thermo Fisher Scientific/Abcam) as described in (Kroschwald et al., 2017). Samples were monitored 0–30 min after infiltration. 0 min after infiltration was used as a control. In each case, the drugs were infiltrated into half leaves of *N. benthamiana* plants that had been agroinfiltrated with FL-P6 three days previously. The other half of the same leaf, which was not treated with drugs, was also examined by microscopy to serve as a control for the drug treatment.

### 3. Results

#### 3.1. P6 IBs are dynamic structures

Previously, we (Lutz et al., 2015) and others (Geldreich et al., 2017; Haas et al., 2005, 2015; Harries et al., 2009; Laird et al., 2013) showed that expression of FL-P6 caused the production of foci (later determined to be inclusion bodies (IBs)) of a variety of sizes and shapes in *N. benthamiana* leaf cells (Fig. 1A). The size distribution (Fig. 1B) showed that the frequency of IBs that were small in size (0.07–1.0  $\mu\text{m}^2$ ) was significantly higher than the large IBs (>5  $\mu\text{m}^2$ ).

FL-P6 IBs are usually spheroidal and can fuse when they are in close proximity (Fig. 1C and D; Movies S1A and S1B). Larger IBs also can dissociate into smaller ones, which suggests that they have liquid properties. The fusion/dissociation of IBs generally represents perhaps 1% of the IBs in any particular time-lapse movie. However, this dissociation property was generally not observed in IBs larger than 5  $\mu\text{m}^2$ . IBs can also be pleomorphic, changing shape before they split during dissociation and regaining their spheroidal shape after fusion (Fig. 1C).

In some cases when IBs come within 1.2–2.2  $\mu\text{m}$  of each other but do not fuse, either when moving into that position, or as a result of dissociation, the two IBs seem to move in a correlated manner as though they are joined together (Fig. 1D, Movie S1B). P6, when examined via the PSPredictor Software (Sun et al., 2019), showed a value of 0.7138. This indicates that P6 has the potential for liquid-liquid phase separation, which makes sense because the protein contains several self-association (Haas et al., 2005; Li and Leisner, 2002) and RNA-binding regions (Cerritelli et al., 1998; De Tapia et al., 1993).

Small ( $\sim\leq 5 \mu\text{m}^2$ ) IBs were disrupted by a 30-min treatment with 1,6-hexanediol (Fig. 1E and F, Movie S2). Before treatment, numerous small IBs are apparent in the white box in Fig. 1E. After the 30-min treatment (Fig. 1F), the small region of the image is almost completely devoid of IBs. Interestingly, large IBs (>5  $\mu\text{m}^2$ ) were not disrupted but were reduced in size by 1,6-hexanediol treatment. For example, large IBs declined in size by about 1.3-fold (32–24  $\mu\text{m}^2$ ; red arrow in Movie S2), 2-fold (59–30  $\mu\text{m}^2$ ; yellow arrow in Movie S2), and 3-fold (91–30  $\mu\text{m}^2$ ; green arrow in Movie S2), respectively in Fig. 1E, F. This may suggest that larger IBs contain a 1,6-hexanediol-resistant, gel-like core with peripheral regions that are sensitive to this solvent.

#### 3.2. P6 deletions lacking individual self-association regions show differing potential to form foci

P6 contains four regions (D1-D4; Fig. 2A) that play a role in P6 self-association (Haas et al., 2005; Li and Leisner, 2002). To investigate the role of these regions in IB formation, P6 mutants were generated in which each of the four regions was individually deleted and fused to GFP. All four deletion mutant proteins were individually expressed in *N. benthamiana* as detected by Western blot analysis (Fig. S1B). Three out of the four deletion mutant proteins produced foci, as did the wild-type protein (Fig. 2B). This suggests that P6 is remarkably resilient to mutation where focus formation is concerned. However, it is still unclear if these foci are authentic IBs. *N. benthamiana* foliar cells expressing P6 $\Delta$ D1-GFP (Fig. 2C) showed diffuse green fluorescence throughout the nucleus, along with several more intensely fluorescing foci. Others have reported similar findings (Geldreich et al., 2017; Haas et al., 2005, 2015; Laird et al., 2013). *N. benthamiana* foliar cells expressing P6 $\Delta$ D2-GFP showed a single, very large, green fluorescent

focus (Fig. 2D). In some respects, this is reminiscent of late stage viral infection, where chronically-infected cells contain a single, large IB near the nucleus (Shepherd, 1976). It seems possible that the  $\Delta D2$  mutation causes enhanced IB fusion, decreased dissociation, or a combination of both, relative to wild-type P6. Interestingly, the large IBs formed by P6 $\Delta D2$ -GFP show a low mobility either the same as, or even less than, the large IBs produced by the full-length protein. P6 $\Delta D2$ -GFP appeared to co-localize with eIF3g (Fig. S1A), indicating that at least some parts of the protein are in a normal conformation. *N. benthamiana* foliar cells expressing P6 $\Delta D3$ -GFP (Fig. 2E) showed mainly a single, large IB ( $>10 \mu\text{m}^2$ ) within each cell expressing this construct, although a few small and intermediate sized ones ( $\sim 0.3 \mu\text{m}^2$ – $5 \mu\text{m}^2$ ) were also occasionally observed. *N. benthamiana* foliar cells expressing P6 $\Delta D4$ -GFP showed a peripheral distribution within plant cells, but fluorescent foci were not observed (Fig. 2F).

### 3.3. Co-expression of actin-binding polypeptides with FL-P6 restricts IB movement and alters size distribution

Small P6-IBs were reported to move rapidly, while large IBs showed restricted mobility (Harries et al., 2009). We also found that the small

IBs ( $0.07$ – $1.0 \mu\text{m}^2$ ) moved rapidly within cells (Movies S1A and S1B). Interestingly, small IBs ( $0.07$ – $1.0 \mu\text{m}^2$ ) appeared to move in a variety of directions, while much larger IBs ( $>5 \mu\text{m}^2$ ), if mobile, moved in a single direction and then did not move again for the rest of the time period examined. A plot of velocity ( $\mu\text{m s}^{-1}$ ) versus size ( $\mu\text{m}^2$  area) showed that small IBs ( $0.07$ – $1.0 \mu\text{m}^2$ ) moved very quickly with velocities as high as  $\sim 30 \mu\text{m s}^{-1}$  (Fig. 3D). The majority of these IBs move between  $2.5 \mu\text{m s}^{-1}$  (threshold value) and  $15 \mu\text{m s}^{-1}$ . Intermediate-sized IBs ( $\sim 1.0$ – $5.0 \mu\text{m}^2$ ) also move rapidly but not to the same upper limit as the smaller ones. Large IBs ( $>5 \mu\text{m}^2$ ) mainly show restricted velocities of  $5 \mu\text{m s}^{-1}$  or less. IBs greater than  $10 \mu\text{m}^2$  were essentially immobile. This last observation was useful as it served as an internal control to set a threshold for categorizing IBs into low (equal to or below the threshold) and high (above threshold) mobility classes. In general, IBs showed a ratio of high to low mobility classes of 60% to 40%, respectively.

Because small IBs were reported to move along actin filaments (Harries et al., 2009), the association of IBs with the actin cytoskeleton was investigated by co-expressing FL-P6 with either LifeAct-mCherry (Fig. S2A) or Talin-DsRed (Fig. S2B). Indeed, we found that small IBs were associated with actin filaments labeled with either LifeAct-mCherry or Talin-DsRed. However, three other observations

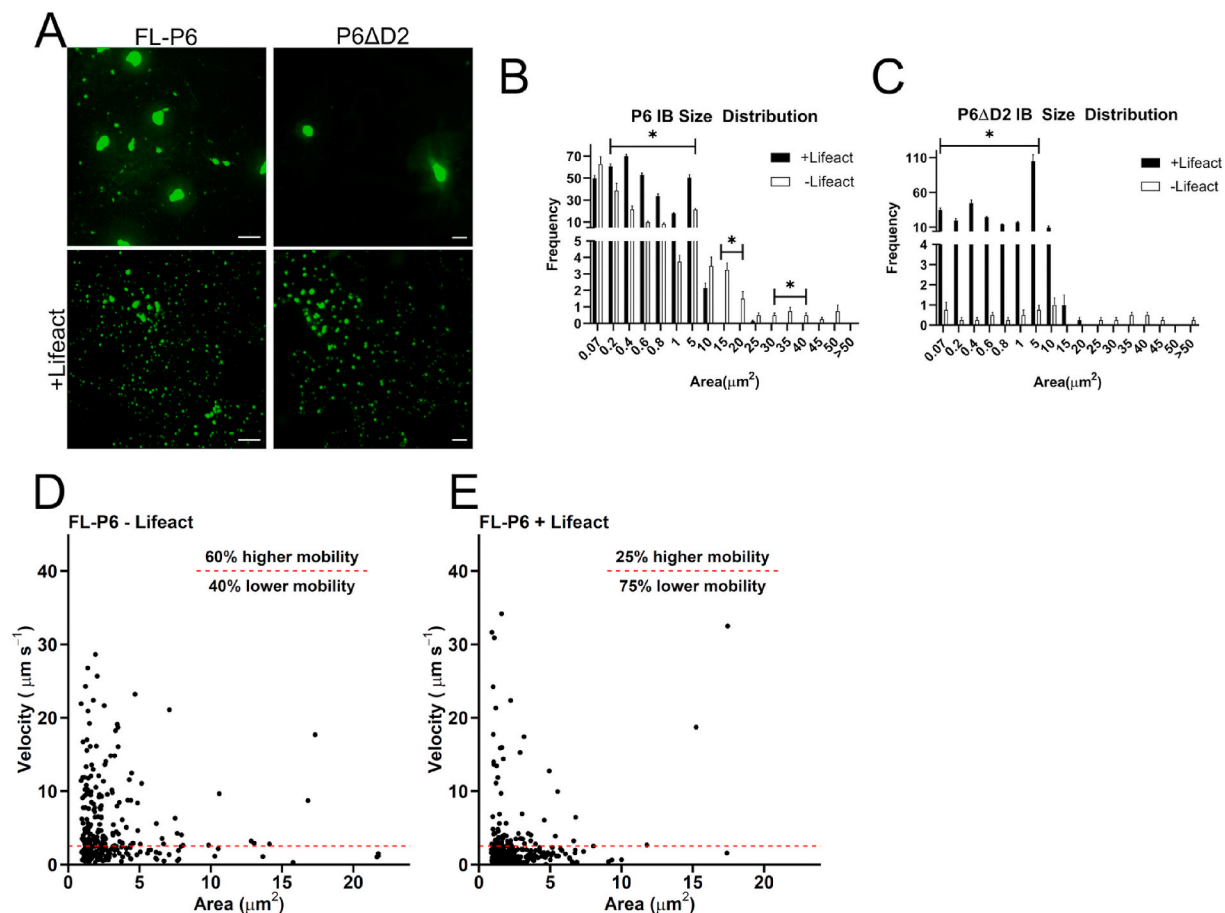


**Fig. 3.** Co-expression of actin-binding proteins with FL-P6 or P6 $\Delta D2$ -GFP influences the size distribution and movement of IBs.

*Nicotiana benthamiana* leaves co-agroinfiltrated with constructs expressing either fluorescent FL-P6 or P6 $\Delta D2$ -GFP with LifeAct-mCherry for three days followed by spinning disc confocal fluorescence microscopy. A. The effects of LifeAct-mCherry on IB formation by FL-P6 and P6 $\Delta D2$ -GFP. Upper left panel, FL-P6 control; lower left panel, FL-P6 co-expressed with LifeAct-mCherry (only green channel is shown, to see expression of both proteins see Fig. S2A); upper right panel, P6 $\Delta D2$ -GFP control; lower right panel, P6 $\Delta D2$ -GFP co-expressed with LifeAct-mCherry (only green channel is shown, to see expression of both proteins see Fig. S2C). All images in A. are Z-Stacks and the scale bars in all images indicate 10  $\mu\text{m}$ . B. Size distribution of FL-P6 IBs under control, white bars; or LifeAct-mCherry co-expression, black bars. Asterisks denote statistically significant differences between LifeAct co-expression and controls for a particular size class ( $P < 0.05$ ) by a paired T-Test. C. Size distribution of P6 $\Delta D2$ -GFP IBs under control, white bars; or LifeAct-mCherry co-expression, black bars. Asterisks denote statistically significant differences between LifeAct co-expression and controls for a particular size class ( $P < 0.05$ ) by a paired T-Test. Velocity plots for FL-P6 under control D., or co-expressed with LifeAct-mCherry E. Dashed red line indicates threshold of movement ( $2.5 \mu\text{m s}^{-1}$ ); below, low mobility; above, high mobility; ratio of low versus high mobility is given in the figure. (For interpretation of the references to color in this figure legend, the reader is referred to the Web version of this article.)

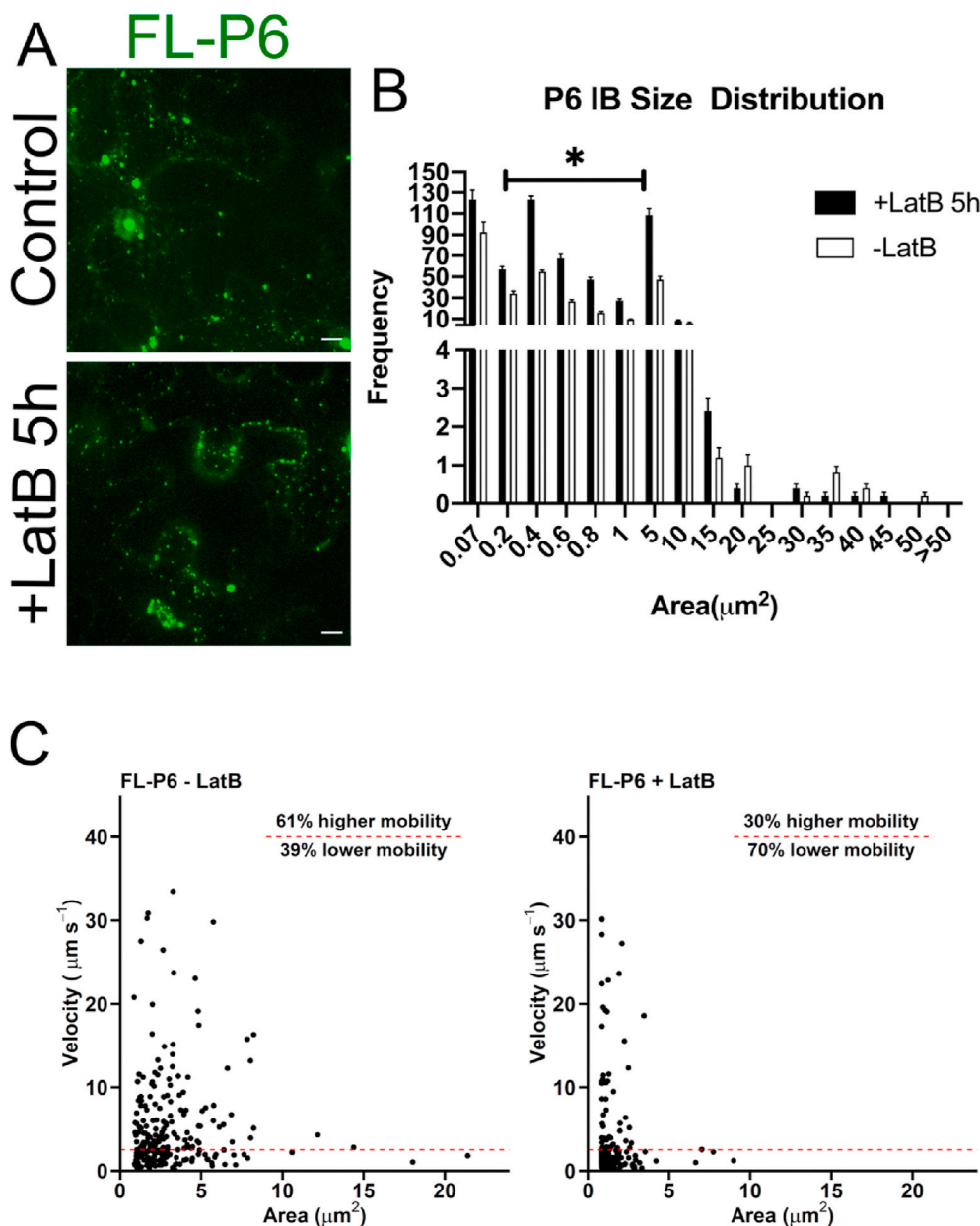


**Fig. 4.** Treatment with actin drugs affects the size distribution and movement of P6 IBs.

*Nicotiana benthamiana* leaves agroinfiltrated with a construction expressing FL-P6 for three days followed by 5 h of drug treatment and imaging by spinning disc confocal fluorescence microscopy. A–C. Latrunculin B (LatB) influences IB formation. A. Upper panel, leaves expressing FL-P6 infiltrated with DMSO (control); lower panel, with LatB. B. Plot of size distribution for control, white bars and LatB treated, black bars; asterisks indicate a significant difference between control and LatB treated for a specific size class with  $P < 0.05$  using a paired T-Test, all other size classes are not significantly different. C. IB velocity plots for control, left panel and LatB treated, right panel. The percentage of IBs showing either high or low mobility is given and the red line indicates the threshold indicating low mobility. The percentage of IBs showing either high or low mobility is given and the red line indicates the threshold indicating low mobility. Scale bars represent 10  $\mu\text{m}$ . (For interpretation of the references to color in this figure legend, the reader is referred to the Web version of this article.)

were made from these experiments. First, IB size was significantly altered (Fig. 3A). Second, IB size distribution was shifted to the smaller end of the spectrum (Fig. 3B). Except for the smallest size class ( $0.07 \mu\text{m}^2$ ), all size classes after that up to  $5 \mu\text{m}^2$  were increased in the plants co-expressing LifeAct-mCherry above what was observed in the control size distribution. The  $10 \mu\text{m}^2$  IB size class was reduced below controls for the LifeAct-mCherry co-expressing leaves. IBs larger than  $10 \mu\text{m}^2$  were not observed. Third, the mobility of IBs was greatly reduced in the LifeAct-mCherry co-expressing leaves (Fig. 3E) compared to controls (Fig. 3D). The small ( $0.07 - 3 \mu\text{m}^2$ ) size classes were still mobile but the mobility of IBs  $> 3 \mu\text{m}^2$  dropped off very rapidly. Furthermore, the mobility ratio changed from 25% higher mobility to 75% lower mobility, compared to 60% and 40% respectively, for controls. One key point that emerges from these data is that when IB mobility is restricted, the size distribution is altered enriching the spectrum towards the smaller size classes.

Similar effects on size (Fig. S2B), size distribution (Fig. S2E) and mobility (Fig. S2G) were observed when FL-P6 was co-expressed with

Talin-DsRed. However, the effects caused by Talin-DsRed were not as extreme as those caused by LifeAct-mCherry. For LifeAct-mCherry and Talin-DsRed both IB fusion and dissociation events were no longer observed, indicating that these activities involve the actin cytoskeleton.

The effects of actin-binding proteins on the size distribution of IBs were even more dramatic on the P6 $\Delta$ D2-GFP deletion mutant. P6 $\Delta$ D2-GFP foci appeared to be associated with the actin cytoskeleton labeled with either LifeAct-mCherry (Fig. S2C) or Talin-DsRed (Fig. S2D). However, instead of producing only a single large IB per cell (Fig. 3A), co-expression of P6 $\Delta$ D2-GFP with mCherry-LifeAct resulted in many small to intermediate-sized IBs and no large ones. This can be seen in the size distribution (Fig. 3C), in which every IB size class smaller than  $5 \mu\text{m}^2$  was significantly enriched in the LifeAct-mCherry co-expressing leaves compared to controls, but IBs  $> 20 \mu\text{m}^2$  were reduced. Interestingly, the small to intermediate-sized IBs observed in the LifeAct-mCherry co-expressing leaves were immobile. As mentioned above for wild type FL-P6, co-expression of P6 $\Delta$ D2-GFP with Talin-DsRed showed similar but less dramatic effects than LifeAct-mCherry (Fig. S2D and S2F).

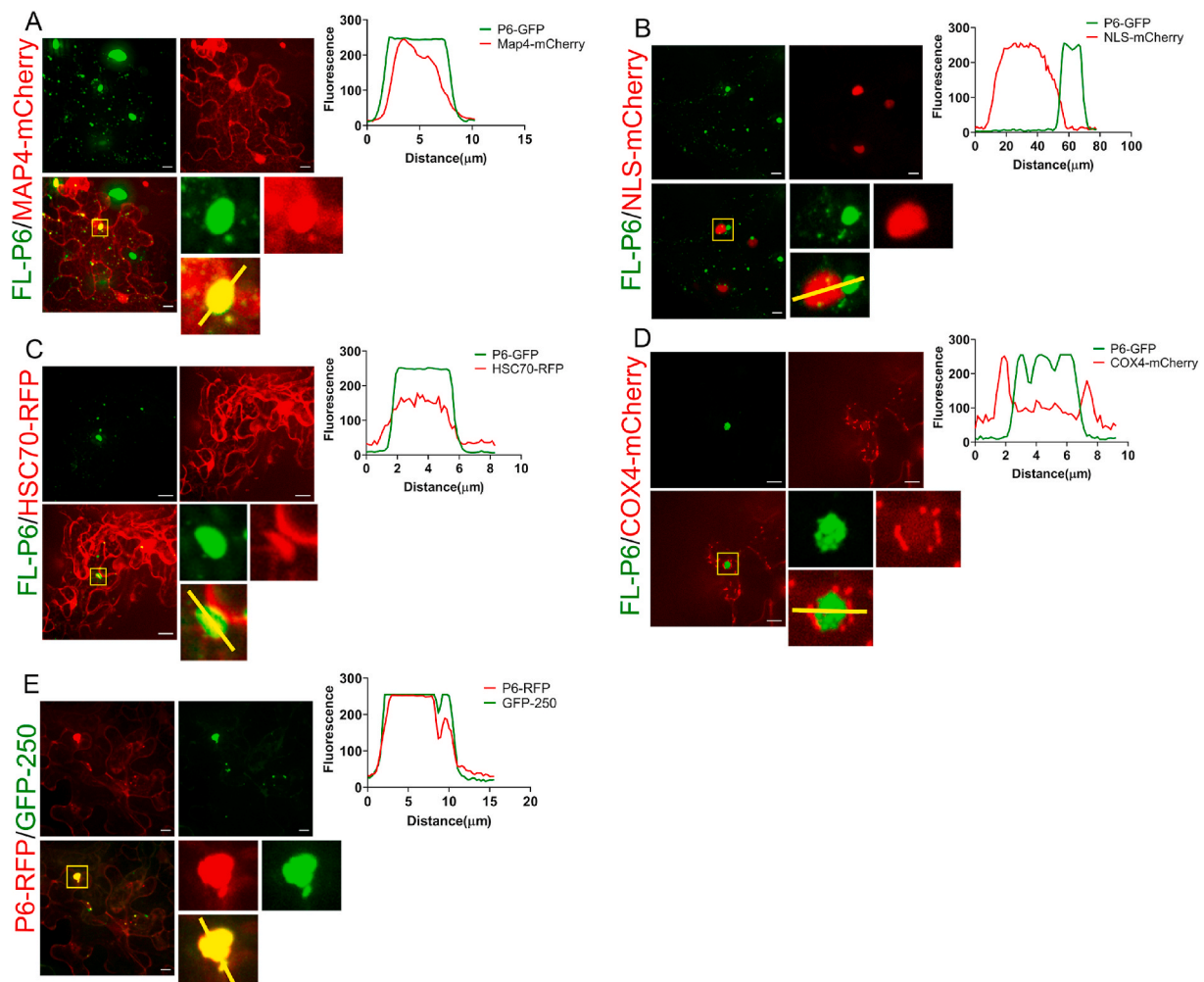


**Fig. 5.** Large P6 IBs are associated with cellular markers of the aggresome pathway.

*Nicotiana benthamiana* leaves agroinfiltrated with a construct expressing fluorescent P6 and cellular markers for three days followed by spinning disc confocal fluorescence microscopy. FL-P6 was co-expressed with cellular markers of the aggresome pathway: A., microtubule marker, MAP4-mCherry; B., nuclear marker, NLS-mCherry; C., HSC70-RFP, cellular heatshock protein; and D., COX4-mCherry, mitochondrial marker. E. P6-RFP co-expressed with GFP-250 animal cell aggresomal marker. For A.-D., Each panel consists of: upper left, image of FL-P6 (green channel); upper center, image of cellular marker (red channel); upper right, fluorescence intensity plot of region indicated by yellow lines in the merged image below. Lower left image, merge of upper left and upper center panels with box indicating area analyzed further. Three images to the bottom right of the panel are magnified views of the boxed area: upper left, FL-P6 (green channel); upper right, cellular marker (red channel); lower left, merged image. E. Upper left panel, P6-RFP (red channel); upper center, GFP-250 (green channel); upper right, fluorescence intensity plot of region indicated by yellow lines in the merged image below. Lower left image, merge of upper left and upper center panels with box indicating area analyzed further. Three images to the bottom right of the panel are magnified views of the boxed area: upper left, P6-RFP (red) channel; upper right, GFP-250 (green channel); lower left, merged image. Images shown are Z-Stacks and scale bars in all images indicate 10  $\mu\text{m}$ . (For interpretation of the references to color in this figure legend, the reader is referred to the Web version of this article.)

### 3.4. Myosin-inhibiting drugs do not affect small IB movement but actin filament polymerization inhibitors do

From the literature (Harries et al., 2009) and our current study, it is clear that the actin cytoskeleton is involved in IB movement. Molecules may move using actin filaments in two ways: either via myosins, or through actin filament polymerization (Cramer et al., 1994; Svitkina, 2018). Two drugs: BDM and BL, were used to examine the potential role of myosins in mitochondrial and IB movement. Mitochondria move within plant cells (Movie S3A) via a myosin-based mechanism and are inhibited when plant cells are treated with BDM (Tominaga et al., 2000; Van Gestel et al., 2002). Thus, mitochondrial movement is a good measure of the effectiveness of these drugs. As expected, treatment with either BDM or BL inhibited mitochondrial movement (Movies S3B and S3C, respectively). However, the kinetics of action for the two drugs was different. Treatment with BDM for 30 min completely abolished mitochondrial movement, while BL treatment required only 10 min to

prevent movement. Thus, these drugs were entering plant cells and interfering with myosin-based mitochondrial movement. Neither BDM (Movie S3D) nor BL (Movie S3E) treatment interfered with the movement of small (up to 1  $\mu\text{m}^2$ ) IBs. The slow movement of IBs  $>5 \mu\text{m}^2$  was not affected by either drug.

Supplementary video related to this article can be found at <https://doi.org/10.1016/j.virol.2020.10.003>

Latrunculin B (LatB) interferes with actin polymerization (Chen et al., 2007). Compared to control, IB appearance was affected by LatB treatment (Fig. 4A). After 5 h of LatB treatment, all size classes, in the size distribution graph (Fig. 4B) below 10  $\mu\text{m}^2$  (except the smallest) were enriched relative to control. The greatest enrichment was observed for the 0.4  $\mu\text{m}^2$  and 5  $\mu\text{m}^2$  size classes. All size classes  $>5 \mu\text{m}^2$  were not significantly different from the controls due to large variability. In contrast with the myosin inhibiting drugs, LatB-treated cells expressing FL-P6 showed a dramatic reduction in movement (Movie S4B) relative to control (Movie S4A). Mobility plots (Fig. 4C) showed that movement

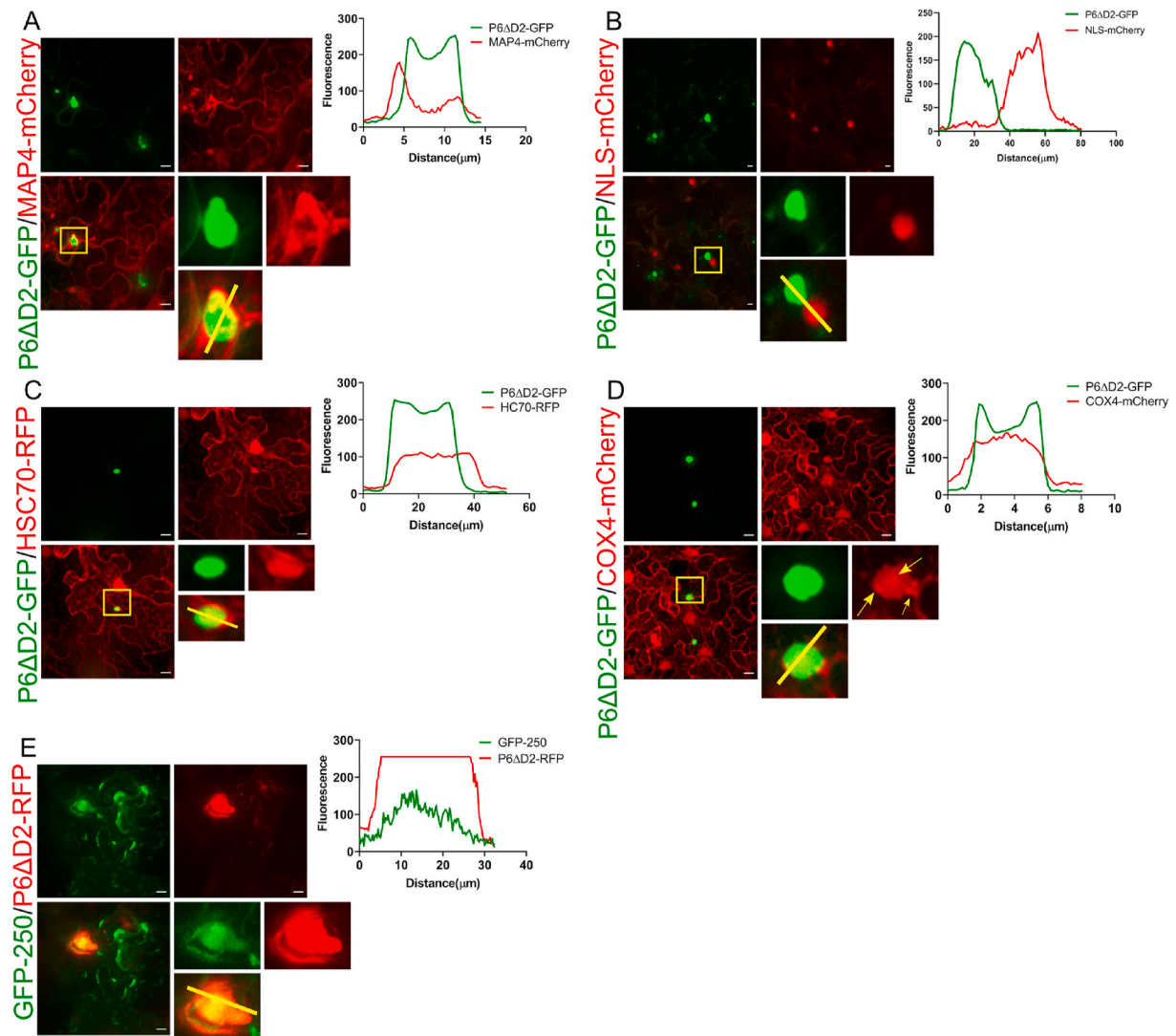


**Fig. 6.** Large IBs formed by P6 $\Delta$ D2 are correlated with aggresome markers.

*Nicotiana benthamiana* leaves agroinfiltrated with a construction expressing fluorescent P6 $\Delta$ D2 and cellular markers for three days followed by spinning disc confocal fluorescence microscopy. P6 $\Delta$ D2 was co-expressed with cellular markers: A. microtubule marker, MAP4-mCherry; B. nuclear marker, NLS-mCherry (20X magnification); C., HSC70-RFP, cellular heatshock protein; and D., COX4-mCherry, mitochondrial marker. E. P6 $\Delta$ D2-RFP co-expressed with GFP-250 animal cell aggresomal marker. For A.-D., Each panel consists of: upper left, image of P6 $\Delta$ D2-GFP (green channel); upper center, image of cellular marker (red channel); upper right, fluorescence intensity plot of region indicated by yellow lines in the merged image below. Lower left image, merge of upper left and upper center panels with box indicating area analyzed further. Three images to the bottom right of the panel are magnified views of the boxed area: upper left, P6 $\Delta$ D2-GFP (green channel); upper right, cellular marker (red channel); lower left, merged image. E. Upper left panel, P6 $\Delta$ D2-RFP (red channel); upper center, GFP-250 (green channel); upper right, fluorescence intensity plot of region indicated by yellow lines in the merged image below. Lower left image, merge of upper left and upper center panels with box indicating area analyzed further. Three images to the bottom right of the panel are magnified views of the boxed area: upper left, P6 $\Delta$ D2-RFP (red channel); upper right, GFP-250 (green channel); lower left, merged image. Images shown are Z-Stacks and scale bars in all images indicate 10  $\mu$ m. (For interpretation of the references to color in this figure legend, the reader is referred to the Web version of this article.)

was inhibited after 5 h of LatB treatment. Only 30% of the IBs were in the higher mobility class and 70% were in the lower mobility class compared to the controls where the numbers were 61% and 39%, respectively. IB movement after LatB treatment was restricted to the smaller size classes (0.7–3  $\mu$ m<sup>2</sup>). However, even the number of small IBs that were mobile was greatly reduced.

### 3.5. Large P6 IBs colocalize with aggresomal markers

Once IBs reach >5  $\mu$ m<sup>2</sup>, they appeared to be associated with the microtubule marker MAP4-mCherry (Fig. 5A) as well as moving more slowly and unidirectionally. Large IBs were found near the nucleus (Fig. 5B) because they co-localized with the nuclear marker NLS-mCherry-GUS, (Ivanov and Harrison, 2014). Together, these data

suggest that large P6-IBs may be formed by the aggresome pathway (Geldreich et al., 2017; Harries et al., 2009; Schoelz and Leisner, 2017). Therefore, large IBs were expected to colocalize with aggresomal markers. Although HSC70-RFP produced a diffuse pattern throughout the cell, it also formed foci, some of which associated with the large (>5  $\mu$ m<sup>2</sup>) IBs formed by FL-P6 (Fig. 5C). Furthermore, the large IBs were surrounded by red fluorescent rod-shaped structures (Fig. 5D) when FL-P6 was co-expressed with mCherry-COX4, a mitochondrial marker. GFP-250 is a useful animal cell marker for aggresomes (Garcia-Mata et al., 1999). When co-expressed with P6-RFP, we observed that GFP foci colocalized with the large (>5  $\mu$ m<sup>2</sup>) IBs formed by P6-RFP (Fig. 5E). Taken together, these data suggest that large FL-P6 IBs appear to be associated with the aggresome pathway.

Our data above showed that P6 $\Delta$ D2-GFP forms only a single large IB

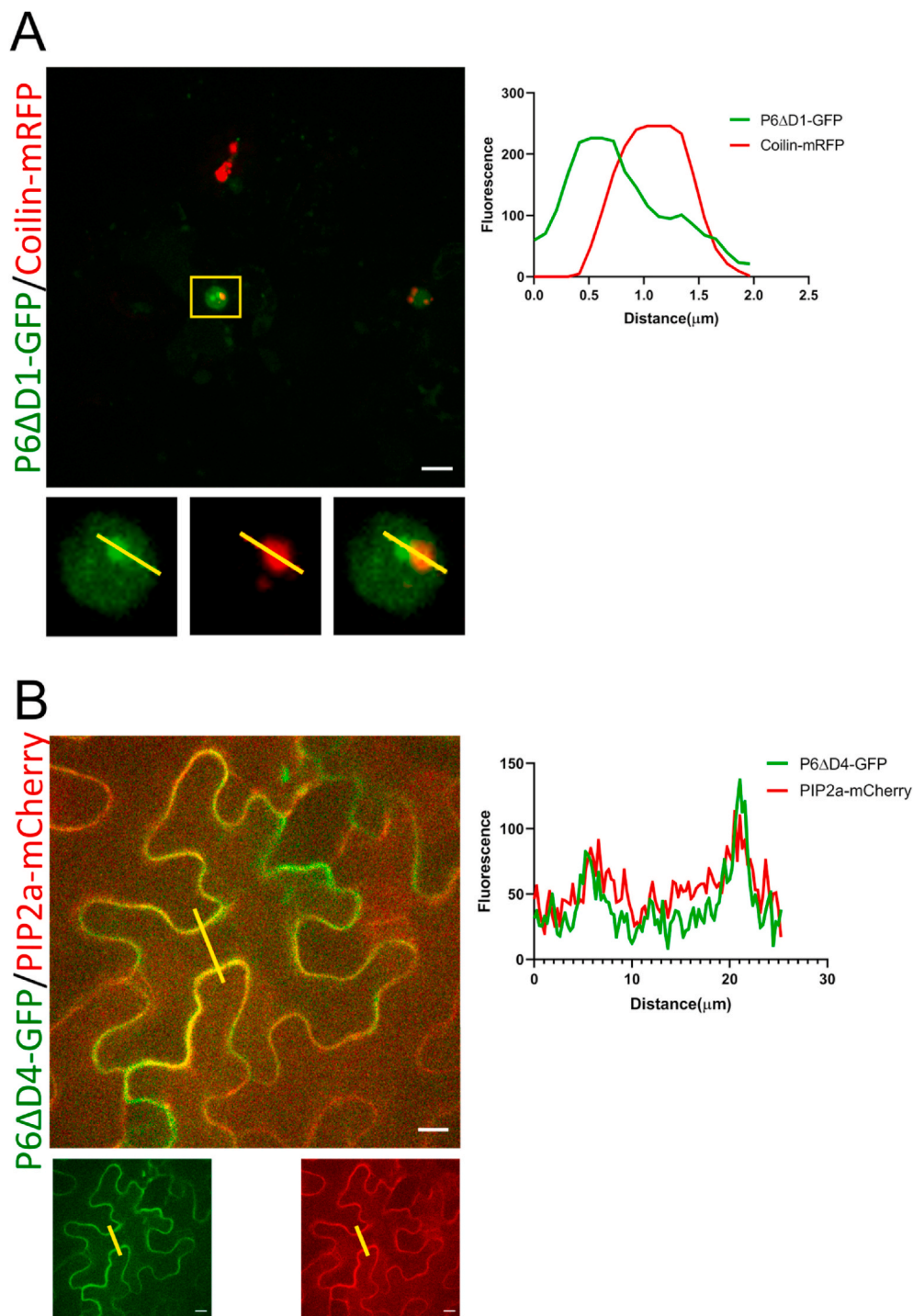


**Fig. 7. Subcellular colocalization of P6 D1 and D4 deletions with plant markers.** *Nicotiana benthamiana* leaves agroinfiltrated with a construction expressing fluorescent P6 deletions and cellular markers for three days followed by spinning disc confocal fluorescence microscopy. A. P6ΔD1-GFP and coilin-mRFP co-expression in *N. benthamiana* leaves. Upper left panel, low magnification Z-Stack of P6ΔD1-GFP and coilin-mRFP co-expression; lower panels, higher magnification images of boxed areas in upper left panel; lower left panel, green channel (P6ΔD1-GFP); lower center panel, red channel (coilin-mRFP); lower right panel, merged image of the lower left and center panels. Upper right panel, fluorescence intensity plot of single plane region indicated by yellow lines in lower images. B. P6ΔD4-GFP and *A. thaliana* PIP2a-mCherry co-expression in *N. benthamiana* leaves. Upper left panel, merged image of co-expression of P6ΔD4-GFP (green channel) lower left image and *A. thaliana* PIP2a-mCherry (red channel) lower right image. Upper right panel, fluorescence intensity plot of single plane region indicated by yellow lines in lower images. Scale bars in all images indicate 10 μm. (For interpretation of the references to color in this figure legend, the reader is referred to the Web version of this article.)

per cell (Fig. 2D), as does P6ΔD2-RFP (Fig. 6E). To investigate if this large IB forms in a manner similar to the large IBs formed by the wild-type protein, co-localization of P6ΔD2-GFP with aggresomal markers was examined. As observed with wild-type, P6ΔD2-GFP was associated with a microtubule marker (Fig. 6A). The large P6ΔD2-GFP IB was localized near the nucleus (Fig. 6B). HSC70-RFP red fluorescent foci co-localized with the large P6ΔD2-GFP IB (Fig. 6C). Furthermore, mitochondria were found around the periphery of the large IB (Fig. 6D). However, they were not as well-organized around the P6ΔD2-GFP IBs as they were around the wild-type IBs. Finally, the large IB formed by P6ΔD2-RFP also co-localized with GFP-250 (Fig. 6E). These data suggest that like the large IBs formed by the wild-type protein, the large P6ΔD2-

GFP IBs are also associated with the aggresome pathway.

### 3.6. P6ΔD1-GFP and P6ΔD4-GFP localize adjacent to cajal body and plasma membrane markers, respectively

As reported previously (Haas et al., 2005, 2015) and indicated above (Fig. 2C), deletion of the N-terminal 110 amino acids from P6 results in nuclear localization. In addition to being distributed throughout the nucleoplasm, small P6 green fluorescent foci were also observed in the nucleus. One possibility was that the foci could be Cajal bodies. To investigate this, co-localization of P6ΔD1-GFP with the Cajal body marker coilin tagged with mRFP (Kim et al., 2007) was examined

(Fig. 7A). Coilin-mRFP expressed alone showed the formation of red fluorescent Cajal bodies within the nucleus (Fig. S3). When co-expressed with P6 $\Delta$ D1-GFP, the coilin-mRFP marker formed foci located adjacent to P6 $\Delta$ D1-GFP foci (Fig. 3A). Fluorescence intensity plots showed an adjacent signal for both proteins. Furthermore, the distribution of coilin-mRFP within the nucleus appeared to be altered by co-expression with P6 $\Delta$ D1-GFP (Fig. S3). In some cases, both coilin-mRFP and P6 $\Delta$ D1-GFP colocalized to what appeared to be the nucleolus, a compartment where coilin on its own is usually not observed (Kim et al., 2007). This suggests that P6 $\Delta$ D1 may interact with coilin in a complex manner.

The peripheral distribution of P6 $\Delta$ D4-GFP suggests a possible membrane association. To investigate this further, we examined the colocalization of P6 $\Delta$ D4-GFP with a plasma membrane marker (*A. thaliana* PIP2a-mCherry) (Ivanov and Harrison, 2014). Co-localization of P6 $\Delta$ D4-GFP with PIP2a-mCherry showed that a portion of the mutant protein was indeed closely associated with the plasma membrane (Fig. 7B). Fluorescence intensity plots also indicate an overlap in signals for both proteins.

#### 4. Discussion

Inclusion bodies generated by many animal and plant viruses are thought to serve a number of roles in the infection process (de Castro et al., 2013; Martelli and Russo, 1977; Moshe and Gorovits, 2012; Novoa et al., 2005). As far as CaMV is concerned, P6 IBs are where viral protein synthesis, genome replication, and virion assembly occur (Schoelz and Leisner (2017) and references therein). Because of their many pro-viral activities, it was important to understand how P6 IBs assemble.

Since P6 is the major constituent of IBs, it provides a useful tool for understanding how these virus-induced structures form. Recent studies showed that labeling P6 with fluorescent proteins permitted visualization of IBs within a cell (Angel et al., 2013; Geldreich et al., 2017; Haas et al., 2005; Harries et al., 2009; Laird et al., 2013; Lutz et al., 2015). As with the other papers, here we show that FL-P6 forms IBs of a variety of sizes. IBs ranged in size (area) from very small ( $\leq 0.07 \mu\text{m}^2$ ) to very large ( $> 50 \mu\text{m}^2$ ). The majority of IBs were in the small size range, with a long-tailed distribution showing very few very large ones. Such a long-tailed distribution could be indicative of preferential attachment (Page, 2018). Thus, newly-synthesized P6 or small IBs may be driven to bind to pre-existing IBs rather than stay on their own.

IBs up to  $5 \mu\text{m}^2$  were very dynamic not only moving within the cell, but also fusing and dissociating. In general, IBs are typically spheroidal in shape, although the shape can change under these dynamic conditions. For example, before an IB separates into two, part of the IB becomes distended before breaking off from the remaining mass. In addition, when two IBs fuse into one, they rapidly regain their spheroidal appearance. To permit such plastic properties, our data suggest that the IBs utilize liquid-liquid phase separation (Alberti and Dormann, 2019; Cuevas-Velazquez and Dinneny, 2018; Hyman et al., 2014). To further support this idea, the major IB constituent, P6, has the hallmarks of a protein capable of liquid-liquid phase separation including being predicted to be capable of this process in silico (Sun et al., 2019). However, not all IBs are entirely liquid. Treatment with 1,6-hexanediol reduces the size of larger ( $> 5 \mu\text{m}^2$ ) IBs. These data suggest that larger IBs have an outer 1,6-hexanediol-sensitive, fluid outer layer and a resistant core. Just such an organization has been reported for other types of membraneless organelles (Alberti and Dormann, 2019).

The fusion-dissociation process that we documented for P6 IBs is likely a type of regulated equilibrium, ultimately favoring the formation of large IBs. Interestingly, this equilibrium apparently can be disrupted by either mutation of P6, or by affecting host cell actin dynamics. P6 contains four regions involved in self-association (Li and Leisner, 2002). Surprisingly, individual deletion of three of these four regions still permitted the mutant P6s to form foci. Whether these foci are actual IBs or merely nonfunctional aggregates has yet to be determined. One can

arrange the deletion mutant P6s into a type of continuum: P6 $\Delta$ D4 is incapable of nucleation to form IBs at all, so it is at one extreme; P6 $\Delta$ D1 forms mainly small IBs (although they are located in the nucleus); P6 $\Delta$ D3 forms mainly several large IBs per cell; and at the other extreme is P6 $\Delta$ D2, which typically forms a single large IB per cell. Wild type P6 fits somewhere in the middle of this continuum for our studies, as it can form IBs of a variety of different sizes. Interestingly, the formation of a single, large IB per cell is a typical cytopathic effect of chronic, late-stage CaMV infection (Shepherd, 1976). Therefore, P6 $\Delta$ D2 forms IBs characteristic of late-stage infection, but it does this in a manner that is greatly accelerated compared to the wild-type protein. It is possible that the fusion-dissociation equilibrium is disrupted by the D2 deletion such that fusion is enhanced, dissociation is reduced, or both. One insight to emerge from these mutant studies is that the extremes of the continuum are marked by P6s lacking D4 at one end and D2 at the other. This is interesting as both of these regions bind with CHUP1 (Angel et al., 2013).

CHUP1 is a chloroplast outer membrane protein that moves chloroplasts within plant cells in response to light conditions and was proposed to mediate this movement via actin filament polymerization (Wada and Kong, 2018). Since P6 interacts with CHUP1, it is possible that IBs also move by actin filament polymerization. Therefore, we investigated if drugs that affect either myosin activity or actin filament polymerization affected IB movement. Drugs that inhibited myosin function had no effect on IB movement, although they strongly impaired mitochondrial movement. In contrast, drugs that prevented actin filament polymerization strongly impaired, but did not abolish, IB movement. Taken together, these data suggest that IBs up to  $\sim 5 \mu\text{m}^2$  move using actin filament polymerization rather than myosins. However, the involvement of myosins different from those responsible for mitochondrial movement in IB movement cannot be ruled out. It is important to keep in mind that the drug studies show effects on IBs that are already preformed. We also observed effects on IB formation when actin-binding polypeptides were co-expressed as the IBs were forming.

When actin-binding polypeptides were co-expressed with FL-P6, small IB ( $< 5 \mu\text{m}^2$ ) movement was greatly restricted, resulting in an accumulation of smaller IBs, a reduction in the number of large ones, and an alteration of the size distribution. Interestingly, co-expression of these same actin-binding polypeptides also resulted in many small IBs formed by P6 $\Delta$ D2-GFP. This suggests that the construction of large IBs apparently goes through an actin-dependent phase and that the large IBs form via a similar mechanism for both wild-type and P6 $\Delta$ D2 mutant proteins. Overall, these data suggest that actin-based movement is required for fusion and growth of IBs.

When IBs reach approximately  $5 \mu\text{m}^2$  in size, their movement and dynamics is greatly reduced. Apparently, their equilibrium is altered to promote fusion and reduce dissociation. Interestingly, the very large ( $> 20 \mu\text{m}^2$ ) IBs were often associated with microtubule proteins and located near the nucleus. Others (Haas et al., 2005; Harries et al., 2009; Shepherd, 1976) have reported similar results. This suggested to us that the large IBs may be associated with the aggresome pathway (Garcia-Mata et al., 1999; Johnston et al., 1998; Kopito, 2000). Indeed, large IBs did appear to colocalize with aggresomal markers. The role of the aggresome pathway in viral infections is somewhat unclear (Wileman, 2007). In some cases, the aggresome pathway causes degradation of viral proteins (Vogel et al., 2007). In other cases, aggresomes appear to help viruses produce replication sites, possibly by concentration of viral components or protecting them against host defenses (Wileman, 2006). Hence, it is possible that the association of the large P6 IBs with the aggresome pathway may be fulfilling similar functions. It is also possible that the perinuclear location permits the large IBs to more effectively capture viral RNAs leaving the nucleus.

During the course of these studies, we discovered that P6 $\Delta$ D1-GFP not only localized to the nucleus, but that it was also found adjacent to foci formed by the Cajal body protein coilin (Kim et al., 2007). Thus, P6 may play a role in regulating the processing of RNAs within plant cells.

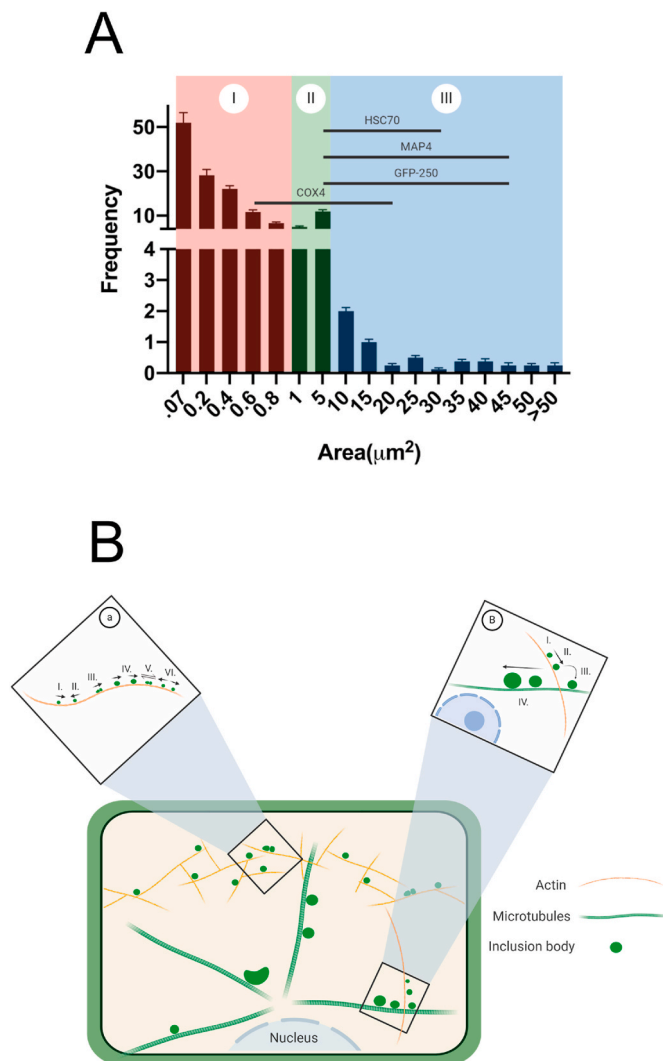


**Fig. 8. Diagram of P6 IB and Dynamics.**

**A.** As a summary, our data show the following co-localizations: **I.** Small IBs ( $0.07 \mu\text{m}^2$ – $1 \mu\text{m}^2$ ) are highly dynamic bodies that show association with mitochondrial marker COX4. **II.** Intermediate inclusions ( $1 \mu\text{m}^2$ – $5 \mu\text{m}^2$ ) are highly dynamic bodies that co-localize with aggresomal markers: HSC70, GFP-250, COX4 and microtubule marker, MAP4. **III.** Large IBs ( $<5 \mu\text{m}^2$ ) are restricted in its movement and show co-localization with aggresomal markers. **B.** IBs are very dynamic and intricate in its formation. Our data suggest: **a.** **I.-II.** Small to intermediate IBs move in a dynamic fashion thru actin filaments where they can encounter other IBs along the way. **III.-IV.** In some cases, IBs that are in close proximity will fuse, forming a bigger IB which will then move. **V.-VI.** Some IBs that have fused previously could dissociate in which each IB will move in different directions. **b.** **I.-III.** Once IBs get to a certain size (Intermediate-Large), it appears that they become less dynamic in its movement and associate with microtubules. **IV.** We hypothesize that IBs that are translocated to microtubules are facilitated by the aggresome pathway. **B.** Adapted from “Round Cell Background (with Cytoskeleton)”, by BioRender.com (2020). Retrieved from <https://app.biorender.com/biorender-templates>.

Interestingly, P6 has been reported to affect the metabolism of tasiRNAs, possibly by interaction with DRB4, or RDR6 (Haas et al., 2015; Shivaprasad et al., 2008). Furthermore the CaMV 35S genomic RNA has been reported to undergo splicing (Bouton et al., 2015). P6 could mediate either or both of these activities by association with Cajal bodies.

In summary CaMV IBs are very dynamic structures (Fig. 8). We defined small IBs ( $\leq 1 \mu\text{m}^2$ ) as high motility structures, the growth of which appears to be governed by two forces, fusion and dissociation.

Both forces are mediated via the actin cytoskeleton and can be disrupted when actin-binding proteins are co-expressed. IBs appear to be a type of membraneless organelle with an inner gel-like core and an outer fluid-like layer distinct from the bulk cytoplasm by liquid-liquid phase separation. This fluid-like outer layer likely assists in small IB fusion/dissociation. Movement of small IBs may be mediated by actin polymerization (Fig. 8A and B). IBs that we classified as intermediate ( $1 \mu\text{m}^2$ – $5 \mu\text{m}^2$ ) demonstrated two types of movement: 1) high mobility, possibly mediated in association with actin, or 2) restricted movement. The intermediate IBs exhibiting restricted movement co-localize with aggresomal markers. Moreover, this type of behavior suggests that once the IBs reach a certain size they appear to be governed by mainly fusion and they hijack the host’s aggresome pathway to move to the nucleus to generate even larger IBs (Fig. 8A and B). Finally, IBs that we categorized as large IBs ( $\geq 5 \mu\text{m}^2$ ) display restricted movement, are commonly located at the periphery of the nucleus and co-localize with aggresomal markers (Fig. 8A and B). Nonetheless, the mechanisms by which these processes are regulated are a focus of our future work. Our current paper investigated the distribution of IBs formed by P6 alone in noninfected cells. Nonetheless, because of the known properties of P6 we would expect the distribution of P6-GFP expressed by agroinfiltration of CaMV-infected leaves to be similar to CaMV-infected cells. For example, P6 self-associates (Haas et al., 2005; Li and Leisner, 2002) and experiments performed with P6-GFP and P6-RFP have shown that the two fluorescent proteins colocalize (Angel et al., 2013). Virus infections express higher levels of P6, than is normally produced by agroinfiltration into leaves. Therefore, we would expect P6-GFP to adopt the pattern exhibited by the viral IBs and to be quite variable because each cell is in a different stage of infection. Collectively, such experiments could be useful to track the progression of small IBs to ultimately the single large IB within a chronically-infected cell. These ideas will be addressed in future experiments that are beyond the scope of the present study

#### CRediT authorship contribution statement

**Roberto Alers-Velazquez:** Experimental design, Investigation, Data analysis, Writing - review & editing. **Sarah Jacques:** Investigation. **Clare Muller:** Data analysis, Reviewing and Editing. **Jennifer Boldt:** Writing - review & editing. **James Schoelz:** Writing - review & editing. **Scott Leisner:** Experimental design, Supervision, Writing - review & editing.

#### Acknowledgements

The authors thank Drs. Bjorn Krenz (Leibniz Institute DSMZ, Department of Virology) and Elizabeth Sztul (Department of Cell Biology, University of Alabama at Birmingham) for the MAP4-mCherry and GFP-250 constructs, respectively. The authors also thank Dr. Qian Chen (Department of Biological Sciences, University of Toledo) for assistance with confocal microscopy, Dr. Wendy Zellner (Department of Biological Sciences, University of Toledo) for her assistance with the manuscript, Taylor Paret (Department of Environmental Sciences, University of Toledo) for assistance with plant growth, and the University of Toledo Plant Science Research Center. This work was supported in part by US Department of Agriculture-Agricultural Research Service Specific Cooperative Agreement (grant number: 58-5082-6-012). Mention of trade names or commercial products in this publication is solely for the purpose of providing specific information and does not imply recommendation or endorsement by the University of Toledo or the U.S. Department of Agriculture. USDA is an equal opportunity provider and employer.

#### Appendix A. Supplementary data

Supplementary data related to this article can be found at <https://doi.org/10.1016/j.virol.2020.10.003>.

## References

- Alberti, S., Dormann, D., 2019. Liquid-liquid phase separation in disease. *Annu. Rev. Genet.* 53, 171–194.
- Angel, C.A., Hsieh, Y.C., Schoelz, J.E., 2011. Comparative analysis of the capacity of tombusvirus P22 and P19 proteins to function as avirulence determinants in Nicotiana species. *Mol. Plant Microbe Interact.* 24, 91–99.
- Angel, C.A., Lutz, L., Yang, X.H., Rodriguez, A., Adair, A., Zhang, Y., Leisner, S.M., Nelson, R.S., Schoelz, J.E., 2013. The P6 protein of Cauliflower mosaic virus interacts with CHUP1, a plant protein which moves chloroplasts on actin microfilaments. *Virology* 443, 363–374.
- Aulas, A., Fay, M.M., Szaflarski, W., Kedersha, N., Anderson, P., Ivanov, P., 2017. Methods to classify cytoplasmic foci as mammalian stress granules. *JoVE* 123, e55656.
- Bak, A., Gargani, D., Macia, J.L., Malouvet, E., Vernerey, M.S., Blanc, S., Drucker, M., 2013. Virus factories of cauliflower mosaic virus are virion reservoirs that engage actively in vector transmission. *J. Virol.* 87, 12207–12215.
- Berardini, T.Z., Reiser, L., Li, D., Mezheritsky, Y., Muller, R., Strait, E., Huala, E., 2015. The Arabidopsis information resource: making and mining the "gold standard" annotated reference plant genome. *Genes* 53, 474–485.
- Bonneville, J.M., Sanfacon, H., Futterer, J., Hohn, T., 1989. Posttranscriptional transactivation in cauliflower mosaic virus. *Cell* 59, 1135–1143.
- Bouton, C., Geldreich, A., Ramel, L., Ryabova, L.A., Dimitrova, M., Keller, M., 2015. Cauliflower mosaic virus transcriptome reveals a complex alternative splicing pattern. *PLoS One* 10, e0132665.
- Bureau, M., Leh, V., Haas, M., Geldreich, A., Ryabova, L., Yot, P., Keller, M., 2004. P6 protein of Cauliflower mosaic virus, a translation reinitiator, interacts with ribosomal protein L13 from Arabidopsis thaliana. *J. Gen. Virol.* 85, 3765–3775.
- Cerritelli, S.M., Fedoroff, O.Y., Reid, B.R., Crouch, R.J., 1998. A common 40 amino acid motif in eukaryotic RNases H1 and caulimovirus ORF VI proteins binds to duplex RNAs. *Nucleic Acids Res.* 26, 1834–1840.
- Chakrabarty, R., Banerjee, R., Chung, S.M., Farman, M., Citovsky, V., Hogenhout, S.A., Tzfira, T., Goodin, M., 2007. PSITE vectors for stable integration or transient expression of autofluorescent protein fusions in plants: probing Nicotiana benthamiana-virus interactions. *Mol. Plant Microbe Interact.* 20, 740–750.
- Chen, T., Teng, N., Wu, X., Wang, Y., Tang, W., Samaj, J., Baluska, F., Lin, J., 2007. Disruption of actin filaments by latrunculin B affects cell wall construction in Picea meyeri pollen tube by disturbing vesicle trafficking. *Plant Cell Physiol.* 48, 19–30.
- Chong, S., Dugast-Darzacq, C., Liu, Z., Dong, P., Dailey, G.M., Cattoglio, C., Heckert, A., Banala, S., Lavis, L., Darzacq, X., Tjian, R., 2018. Imaging dynamic and selective low-complexity domain interactions that control gene transcription. *Science* 361.
- Cramer, L.P., Mitchison, T.J., Theriot, J.A., 1994. Actin-dependent motile forces and cell motility. *Curr. Opin. Cell Biol.* 6, 82–86.
- Cuevas-Velazquez, C.L., Dinnen, J.R., 2018. Organization out of disorder: liquid-liquid phase separation in plants. *Curr. Opin. Plant Biol.* 45, 68–74.
- Daubert, S., Shepherd, R.J., Gardner, R.C., 1983. Insertional mutagenesis of the cauliflower mosaic virus genome. *Gene* 25, 201–208.
- de Castro, I.F., Volonte, L., Risco, C., 2013. Virus factories: biogenesis and structural design. *Cell Microbiol.* 15, 24–34.
- De Tapia, M., Himmelbach, A., Hohn, T., 1993. Molecular dissection of the cauliflower mosaic virus translation transactivator. *EMBO J.* 12, 3305–3314.
- Espinosa, A.M., Medina, V., Hull, R., Markham, P.G., 1991. Cauliflower mosaic virus gene II product forms distinct inclusion bodies in infected plant cells. *Virology* 185, 337–344.
- Feng, Z., Xue, F., Xu, M., Chen, X., Zhao, W., Garcia-Murria, M.J., Mingarro, I., Liu, Y., Huang, Y., Jiang, L., Zhu, M., Tao, X., 2016. The ER-membrane Transport system is critical for intercellular trafficking of the Nsm movement protein and Tomato spotted wilt tospovirus. *PLoS Pathog.* 12, e1005443.
- Fujisawa, I., Hayashi, T., Matsui, C., 1967. Electron microscopy of mixed infections with two plant viruses. I. Intracellular interactions between tobacco mosaic virus and tobacco etch virus. *Virology* 33, 70–76.
- Garcia-Mata, R., Bebock, Z., Sorscher, E.J., Sztul, E.S., 1999. Characterization and dynamics of aggresome formation by a cytosolic GFP-chimera. *J. Cell Biol.* 146, 1239–1254.
- Gardner, R.C., Howarth, A.J., Hahn, P., Brown-Luedi, M., Shepherd, R.J., Messing, J., 1981. The complete nucleotide sequence of an infectious clone of cauliflower mosaic virus by M13mp7 shotgun sequencing. *Nucleic Acids Res.* 9, 2871–2888.
- Geldreich, A., Haas, G., Kubina, J., Bouton, C., Tanguy, M., Erhardt, M., Keller, M., Ryabova, L., Dimitrova, M., 2017. Formation of large viroplasm and virulence of Cauliflower mosaic virus in turnip plants depend on the N-terminal EKI sequence of viral protein TAV. *PLoS One* 12, e0189062.
- Gowda, S., Wu, F.C., Scholthof, H.B., Shepherd, R.J., 1989. Gene VI of figwort mosaic virus (caulimovirus group) functions in posttranscriptional expression of genes on the full-length RNA transcript. *Proc. Natl. Acad. Sci. U. S. A.* 86, 9203–9207.
- Haas, G., Azevedo, J., Moissiard, G., Geldreich, A., Humber, C., Bureau, M., Fukuhara, T., Keller, M., Voinnet, O., 2015. Nuclear import of CaMV P6 is required for infection and suppression of the RNA silencing factor DRB4. *EMBO J.* 34, 2591–2592.
- Haas, M., Bureau, M., Geldreich, A., Yot, P., Keller, M., 2002. Cauliflower mosaic virus: still in the news. *Mol. Plant Pathol.* 3, 419–429.
- Haas, M., Geldreich, A., Bureau, M., Dupuis, L., Leh, V., Vetter, G., Kobayashi, K., Hohn, T., Ryabova, L., Yot, P., Keller, M., 2005. The open reading frame VI product of Cauliflower mosaic virus is a nucleocytoplasmic protein: its N terminus mediates its nuclear export and formation of electron-dense viroplasms. *Plant Cell* 17, 927–943.
- Hadley, W., 2016. Ggplot2. Springer Science+Business Media, LLC, New York, NY.
- Haglund, C.M., Welch, M.D., 2011. Pathogens and polymers: microbe-host interactions illuminate the cytoskeleton. *J. Cell Biol.* 195, 7–17.
- Harries, P.A., Palanichelvam, K., Yu, W., Schoelz, J.E., Nelson, R.S., 2009. The cauliflower mosaic virus protein P6 forms motile inclusions that traffic along actin microfilaments and stabilize microtubules. *Plant Physiol.* 149, 1005–1016.
- Hohn, T., Rothnie, H., 2013. Plant pararetroviruses: replication and expression. *Curr. Opin. Virol.* 3, 621–628.
- Holzinger, A., Blasas, K., 2016. Actin-dynamics in plant cells: the function of actin-perturbing substances: jasplakinolide, chondramides, phalloidin, cytochalasins, and latrunculins. *Methods Mol. Biol.* 1365, 243–261.
- Hull, R., Covey, S.N., 1985. Cauliflower mosaic virus: pathways of infection. *Bioessays* 3, 160–163.
- Hyman, A.A., Weber, C.A., Julicher, F., 2014. Liquid-liquid phase separation in biology. *Annu. Rev. Cell Dev. Biol.* 30, 39–58.
- Ivanov, S., Harrison, M.J., 2014. A set of fluorescent protein-based markers expressed from constitutive and arbuscular mycorrhiza-inducible promoters to label organelles, membranes and cytoskeletal elements in Medicago truncatula. *Plant J.* 80, 1151–1163.
- Johnston, J.A., Ward, C.L., Kopito, R.R., 1998. Aggresomes: a cellular response to misfolded proteins. *J. Cell Biol.* 143, 1883–1898.
- Khelifa, M., Journou, S., Krishnan, K., Gargani, D., Esperandieu, P., Blanc, S., Drucker, M., 2007. Electron-lucent inclusion bodies are structures specialized for aphid transmission of cauliflower mosaic virus. *J. Gen. Virol.* 88, 2872–2880.
- Khelifa, M., Masse, D., Blanc, S., Drucker, M., 2010. Evaluation of the minimal replication time of Cauliflower mosaic virus in different hosts. *Virology* 396, 238–245.
- Kim, S.H., Ryabov, E.V., Kalinina, N.O., Rokitina, D.V., Gillespie, T., MacFarlane, S., Haupt, S., Brown, J.W., Taliansky, M., 2007. Cajal bodies and the nucleolus are required for a plant virus systemic infection. *EMBO J.* 26, 2169–2179.
- Kobayashi, K., Hohn, T., 2004. The avirulence domain of Cauliflower mosaic virus transactivator/viroplasm is a determinant of viral virulence in susceptible hosts. *Mol. Plant Microbe Interact.* 17, 475–483.
- Kobayashi, K., Tsuge, S., Nakayashiki, H., Mise, K., Furusawa, I., 1998. Requirement of cauliflower mosaic virus open reading frame VI product for viral gene expression and multiplication in turnip protoplasts. *Microbiol. Immunol.* 42, 377–386.
- Kopito, R.R., 2000. Aggresomes, inclusion bodies and protein aggregation. *Trends Cell Biol.* 10, 524–530.
- Kovacs, M., Toth, J., Hetenyi, C., Malnasi-Csizmadia, A., Sellers, J.R., 2004. Mechanism of blebbistatin inhibition of myosin II. *J. Biol. Chem.* 279, 35557–35563.
- Krapp, S., Schuy, C., Greiner, E., Stephan, I., Alberter, B., Funk, C., Marschall, M., Wege, C., Bailer, S.M., Kleinow, T., Krenz, B., 2017. Begomoviral movement protein effects in human and plant cells: towards new potential interaction partners. *Viruses* 9.
- Kroschwald, S., Maharana, S., Simon, A., 2017. Hexanediol: a chemical probe to investigate the material properties of membrane-less compartments. *Matters*. <https://doi.org/10.19185/matters.201702000010>.
- Labno, C., 2020. Basic Intensity Quantification with ImageJ. University of Chicago, University of Geneva.
- Laird, J., McNally, C., Carr, C., Doddiah, S., Yates, G., Chrysanthou, E., Khattab, A., Love, A.J., Geri, C., Sadanandom, A., Smith, B.O., Kobayashi, K., Milner, J.J., 2013. Identification of the domains of cauliflower mosaic virus protein P6 responsible for suppression of RNA silencing and salicylic acid signalling. *J. Gen. Virol.* 94, 2777–2789.
- Leh, V., Yot, P., Keller, M., 2000. The cauliflower mosaic virus translational transactivator interacts with the 60S ribosomal subunit protein L18 of Arabidopsis thaliana. *Virology* 266, 1–7.
- Li, J., Leisner, S.M., Frantz, J., 2008. Alleviation of copper toxicity in Arabidopsis thaliana by silicon addition to hydroponic solutions. *J. Am. Soc. Hortic. Sci.* 133, 670–677.
- Li, Y., Leisner, S.M., 2002. Multiple domains within the Cauliflower mosaic virus gene VI product interact with the full-length protein. *Mol. Plant Microbe Interact.* 15, 1050–1057.
- Lutz, L., Okenka, G., Schoelz, J., Leisner, S., 2015. Mutations within A 35 amino acid region of P6 influence self-association, inclusion body formation, and Caulimovirus infectivity. *Virology* 476, 26–36.
- Martelli, G.P., Castellano, M.A., 1971. Light and electron microscopy of the intracellular inclusions of cauliflower mosaic virus. *J. Gen. Virol.* 13, 133–140.
- Martelli, G.P., Russo, M., 1977. Plant virus inclusion bodies. *Adv. Virus Res.* 21, 175–266.
- Martiniere, A., Gargani, D., Uzeit, M., Lautredou, N., Blanc, S., Drucker, M., 2009. A role for plant microtubules in the formation of transmission-specific inclusion bodies of Cauliflower mosaic virus. *Plant J.* 58, 135–146.
- Mattanovich, D., Ruker, F., Machado, A.C., Laimer, M., Regner, F., Steinkellner, H., Himmler, G., Katinger, H., 1989. Efficient transformation of Agrobacterium spp. by electroporation. *Nucleic Acids Res.* 17, 6747.
- Melcher, U., Steffens, D.L., Lyttle, D.J., Lebourier, G., Lin, H., Choe, I.S., Essenberg, R.C., 1986. Infectious and non-infectious mutants of cauliflower mosaic virus DNA. *J. Gen. Virol.* 67 (Pt 7), 1491–1498.
- Moshe, A., Gorovits, R., 2012. Virus-induced aggregates in infected cells. *Viruses* 4, 2218–2232.
- Newby, J.M., Schaefer, A.M., Lee, P.T., Forest, M.G., Lai, S.K., 2018. Convolutional neural networks automate detection for tracking of submicron-scale particles in 2D and 3D. *Proc. Natl. Acad. Sci. U. S. A.* 115, 9026–9031.
- Novoa, R.R., Calderita, G., Arranz, R., Fontana, J., Granzow, H., Risco, C., 2005. Virus factories: associations of cell organelles for viral replication and morphogenesis. *Biol. Cell.* 97, 147–172.

- Page, S.E., 2018. *The Model Thinker : what You Need to Know to Make Data Work for You*, first ed. Basic Books, New York.
- Park, H.-S., Himmelbach, A., Browning, K.S., Hohn, T., Ryabova, L.A., 2001. A plant viral “reinitiation” factor interacts with the host translational machinery. *Cell* 106, 723–733.
- R-Core, 2020. *R: A Language and Environment for Statistical Computing*. R Foundation for Statistical Computing.
- Samaj, J., Peters, M., Volkmann, D., Baluska, F., 2000. Effects of myosin ATPase inhibitor 2,3-butanedione 2-monoxime on distributions of myosins, F-actin, microtubules, and cortical endoplasmic reticulum in maize root apices. *Plant Cell Physiol.* 41, 571–582.
- Schindelin, J., Arganda-Carreras, I., Frise, E., Kaynig, V., Longair, M., Pietzsch, T., Preibisch, S., Rueden, C., Saalfeld, S., Schmid, B., Tinevez, J.Y., White, D.J., Hartenstein, V., Eliceiri, K., Tomancak, P., Cardona, A., 2012. Fiji: an open-source platform for biological-image analysis. *Nat. Methods* 9, 676–682.
- Schoelz, J.E., Leisner, S., 2017. Setting up shop: the Formation and function of the viral factories of cauliflower mosaic virus. *Front. Plant Sci.* 8, 1832.
- Shepherd, R.J., 1976. DNA viruses of higher plants. *Adv. Virus Res.* 20, 305–339.
- Shivaprasad, P.V., Rajeswaran, R., Blevins, T., Schoelz, J., Meins Jr., F., Hohn, T., Pooggin, M.M., 2008. The CaMV transactivator/viroplasm interferes with RDR6-dependent trans-acting and secondary siRNA pathways in Arabidopsis. *Nucleic Acids Res.* 36, 5896–5909.
- Shockey, M.W., Gardner Jr., C.O., Melcher, U., Essenberg, R.C., 1980. Polypeptides associated with inclusion bodies from leaves of turnip infected with cauliflower mosaic virus. *Virology* 105, 575–581.
- Sun, T., Li, Q., Xu, Y., Zhang, Z., Lai, L., Pei, J., 2019. Prediction of liquid-liquid phase separation proteins using machine learning. *bioRxiv*. <https://doi.org/10.1101/842336>.
- Svitkina, T., 2018. The actin cytoskeleton and actin-based motility. *Cold Spring Harb. Perspect. Biol.* 10.
- Tominaga, M., Nakano, A., 2012. Plant-specific myosin XI, a molecular perspective. *Front. Plant Sci.* 3, 211.
- Tominaga, M., Yokota, E., Sonobe, S., Shimmen, T., 2000. Mechanism of inhibition of cytoplasmic streaming by a myosin inhibitor, 2,3-butanedione monoxime. *Protoplasma* 213, 46–54.
- Turner, D.S., McCallum, D.G., Covey, S.N., 1996. Roles of the 35S promoter and multiple overlapping domains in the pathogenicity of the pararetrovirus cauliflower mosaic virus. *J. Virol.* 70, 5414–5421.
- Van Gestel, K., Kohler, R.H., Verbelen, J.P., 2002. Plant mitochondria move on F-actin, but their positioning in the cortical cytoplasm depends on both F-actin and microtubules. *J. Exp. Bot.* 53, 659–667.
- Vogel, F., Hofius, D., Sonnewald, U., 2007. Intracellular trafficking of Potato leafroll virus movement protein in transgenic Arabidopsis. *Traffic* 8, 1205–1214.
- Wada, M., Kong, S.G., 2018. Actin-mediated movement of chloroplasts. *J. Cell Sci.* 131.
- Wileman, T., 2006. Aggresomes and autophagy generate sites for virus replication. *Science* 312, 875–878.
- Wileman, T., 2007. Aggresomes and pericentriolar sites of virus assembly: cellular defense or viral design? *Annu. Rev. Microbiol.* 61, 149–167.